Modeling Velocity Dispersion In Gypsy Site, Oklahoma

by

Sami Ibrahim Alsaadan

B.S. Geophysics
B.S. Economics
University of Tulsa, 2005

SUBMITTED TO THE DEPARTMENT OF EARTH, ATMOSPHERIC AND PLANETARY SCIENCES
IN PARTIAL FULFILLMENT OF THE REQUIREMENTS FOR THE DEGREE OF

MASTER OF SCIENCE IN GEOPHYSICS
AT THE
MASSACHUSETTS INSTITUTE OF TECHNOLOGY

SEPTEMBER 2010

Signature of Author:_____

Earth, Atmospheric and Planetary sciences
September, 7, 2010

Certified by:_____

M. Nafi Toksöz
Professor of Geophysics
Thesis Supervisor

Certified by:_____

Daniel R. Burns
ERL Executive Director / Research Scientist
Thesis Co-Advisor

Accepted by:_____

Maria T. Zuber
E.A. Griswold Professor of Geophysics and Planetary Science
Department Head

Modeling Velocity Dispersion In Gypsy Site, Oklahoma

by

Sami Ibrahim Alsaadan

Submitted to the Department of Earth, Atmospheric and Planetary Sciences

on September, 6, 2010 in partial fulfillment of the

requirements for the Degree of Master of Science in Geophysics

Abstract

Discrepancies in interval velocities estimated from vertical well measurements made with different source central frequencies at Gypsy site could be primarily explained in terms of intrinsic attenuation. Four intervals were chosen for this study based on varying rock properties. The first interval is predominantly shale, second interval is mostly sandstone, and the third interval is made up of shale and sandstone. The fourth interval is the second and third intervals combined. The data used are acquired from three seismic sources; Full Wave Sonic (FWS), Bender log, and Vertical Seismic Profile (VSP) with estimated central frequencies 10kHz, 1kHz, and 100Hz, respectively. The modeling was done using the Discrete Wavenumber (DWN) method and the Logarithmic Dispersion Relation (LDR) to calculate a constant Quality Factor (Q) that best explains the observed velocity dispersion for each of the intervals of interest. The elastic scattering component of the dispersion is negligible. Intrinsic quality factors of 54,35,28, and 30 best explain the field data for first, second, third, and fourth intervals, respectively. The identification and subsequent modeling of velocity dispersion and its components provide key information for integrated reservoir characterization and better enable the prediction of the seismic response at different frequencies.

Thesis Supervisor: M. Nafi Toksöz

Title: Professor of Geophysics

Thesis Co-Advisor: Daniel R. Burns

Title: ERL Executive Director / Research Scientist

Acknowledgements

First and foremost, I am forever grateful to my advisor Professor Nafi Toksöz for admitting me and giving me a chance to study and do research at MIT. Having him as an advisor was truly a privilege. The amounts of support, knowledge, and encouragement I received from him were limitless. He was always available to listen and give advice on academic and personal issues. I always leave with a smile and a positive outlook after any meeting with him.

I am very thankful to my thesis co-advisor Daniel Burns for the knowledge and encouragement he continuously provided me with. He was always supportive and willing to explain and address any concerns or problems I had with my research no matter how trivial or basic they were. The enthusiasm and passion he showed towards my research greatly sparked my interest in the subject I worked on and Geophysics in general.

I thank Professor Allison Malcolm for her constructive feedback on my thesis and for accepting to be in my defense committee on short notice. I am very grateful to Dr. Michel Bouchon for helping me understand the DWN method and for the code he provided to model my data. I am extremely appreciative of the help, advice, and friendship of Dr. Sadi Kuleli and I thank him for being always available to spend as much time as it takes to answer my questions. I would also like to thank and acknowledge the professors who taught me at MIT; Rob van der Hilst, Dale Morgan, Stéphane Rondenay, Allison Malcolm, Bryan Evans, and others.

I thank **all** my colleagues at ERL for being very welcoming and supportive. A special

thanks goes to my office mates throughout my stay; Sudish Bakku, Diego Concha, Xinding Fang, Junlun Li, Bongani Mashele, Nasruddin Nazerali, Di Yang, Fred Pearce and Xin Zhan. I consider myself fortunate to have met them and I value their friendship. I thank Yang Zhang for helping me to understand ERL's Finite Difference codes and Fuxian Song for his input on DWN code. I would also like to thank my collegue and friend at the University of Tulsa and now at MIT, Abdulaziz Almuhaidib, for the help and suggestions he provided during my research and for helping me calculate Finite Difference solutions to compare with them with the DWN. I am also very thankful to my other friends at MIT and Boston for making my stay enjoyable and memorable.

Many thanks go to EAPS administration. I thank Carol Sprague, Susan Turbak, and Linda Meinke for all the help they provided me from the moment I got admitted to the moment I graduated.

I thank Saudi Aramco Oil Company for the full scholarships they gave me during my undergraduate and graduate studies. I'm hopeful that I will utilize the knowledge I accumulated through their sponsorships and contribute back to the company. I thank Dr. Panos Kelamis who was the division head where I worked for the guidance and motivation and for writing the recommendation letter to MIT. I also thank my advisor at Aramco Services Company Reem Alghanim for being very understanding, patient, and supportive.

Finally, no amount of appreciation is sufficient to convey my deepest gratitude and thankfulness towards my family for the love, time, and guidance they continuously gave me. I can only hope and pray to make them proud. I dedicate this thesis to my late grandfather.

Contents

List of Figures

List of Tables

a: Fundamental frequency

API: American Petroleum Institute (units)

Bender: A special tool with a central frequency of either 1kHz or 2kHz designed by NER

DFT: Discrete Fourier Transform

DWN: Discrete Wavenumber method

FFT: Fast Fourier Transform

FWS: Full wave sonic

Interval One: 20.4m thick, predominantly shale, part of the Vamoosa formation, and located above the Gypsy Sandstone formation between 239.1m 259.5m

Interval Two: 23m thick, predominantly sandstone, referred to informally as Gypsy Sandstone, and located between 281.6m to 304.6m

Interval Three: 17.7 thick, composed of shale and sandstone, and located between 304.7m to 322.4m

Interval Four: 40.7m thick, is essentially the second and third interval combined (treated as one formation)

k: Wavenumber

L : Periodic source interval length

LDR: Logarithmic Dispersion Relation

NER: New England Research, Inc.

Q: Quality factor

V: Velocity

VSP: Vertical Seismic Profile

γ : Euler's constant.

ω: Frequency

$\omega_{\mathbf{r}}$: Reference frequency

$\omega_{\mathbf{I}}$: Imaginary part of the frequency

$\mathbf{c}(\omega)$: Velocity

$\alpha(\omega)$: Attenuation factor

H : Hilbert transform

Chapter 1

Introduction

Seismic velocity dispersion and attenuation processes are a direct consequence of earth's inelasticity. Waves propagating in an attenuative medium exhibit amplitude loss and phase change in the seismic wavelet due to the attenuation constant and phase velocity dependence on frequency (Varela et al., 1993). This velocity dependence on frequency (dispersion) is a product of the energy causality when attenuation is present (Futterman, 1962). Higher frequencies travel faster and get attenuated more rapidly than lower frequencies.

In one hand, attenuation and dispersion significantly contribute in distorting the resolution of the seismic image especially in highly anelastic zones; a common approach of processing these distortions is minimum phase-deconvolution. On the other hand, these processes are dependent on the properties of the rocks (e.g. porosity, permeability, fluids, gas, fractures... etc) the waves travel through. Thus, the identification and subsequent modeling and separation of the components of velocity dispersion provide key information in integrated reservoir characterization and predicting the seismic response at different frequencies.

The first attempts to model attenuation mechanisms were based on different adaptations of Hook's law (Sun et al., 2009). Zener (1948) showed through linear solid models that the internal friction occurs at the central peak frequency. Knopoff and MacDonald (1958) made laboratory experiments on stress waves propagating in solids and showed that the transmis-

sion of elastic energy exhibits dissipation even when amplitudes are very small. Schoenberger and Levin (1974) showed through synthetic seismograms that intrabed multiples cause an apparent attenuation. White (1975) demonstrated through lab experiments on partially gas saturated unconsolidated sand an increase of 20% of the compressional wave velocity (1-100Hz) and an attenuation increment of 55db/1000ft (31-123Hz). Klimentos (1995) estimated quality factors for the compressional and shear waves from full wave sonic logs and showed that their ratio could be used as a tool in distinguishing between gas, oil, condensate and water formations.

Spencer (1981) showed through lab experiments that fluid-filled rocks show strong frequency dependency while dry-vacuumed rocks produced practically negligible attenuation and modulus dispersion. Numerous other laboratory and field studies done on velocity dispersion under different rock properties conditions conclude that attenuation and dispersion are linked to reservoir properties (e.g Melia et al., 1984; Winkler, 1986; Doyle et al., 1992; Marion et al., 1994; Yamamato et al., 1994; Brown and Seifert, 1995; Mukerji et al., 1995; Mavko,1998; Johnson, 2001; Pride and Berryman, 2003; Brajanovski et al.,2006; Batzle et al., 2006; Sun et al., 2009).

The main objective of this thesis is to show, model and explain the observed interval velocity discrepancies estimated from well logs at Gypsy site in Oklahoma. We will focus our modeling efforts on four intervals chosen based on varying rock properties such as lithology, porosity, density, and thickness. The first interval is predominantly shale, the second interval is mostly sandstone, and the third interval is made up of shale and sandstone. The fourth interval is essentially interval two and three combined and treated as one formation. The velocity data we use were acquired from three seismic sources; Full Wave Sonic (FWS), Bender, and Vertical Seismic Profile (VSP) with central frequencies of 10kHz, 1kHz, and 100Hz, respectively. We also use gamma, porosity and density logs in modeling and analyzing the results. We model the data using the Discrete Wavenumber (DWN) method and the logarithmic dispersion relation (LDR). Ultimately, we want to develop a framework to

calculate a constant Quality Factor (Q) that best explains the observed velocity dispersion for each of the intervals of interest. We also want to separate and estimate the components of the dispersion in terms of intrinsic attenuation and elastic scattering and find a Q value for each mechanism if both are contributing to the dispersion.

This thesis consists of five chapters and two appendices (including the introduction). Chapter 2 deals with presenting the theoretical background of the DWN and LDR methods and the framework for applying them jointly to model velocity dispersion. A brief discussion of the code used and a generalized workflow are also included. Technical details on the code used are in Appendix A.

Chapter 3 is a presentation and discussion of the data for the site as a whole and for the intervals of interest in particular. It includes a brief introduction, history and geology of the Gypsy test site followed by the technical aspects of data acquisition for each of the three seismic sources we will be using. The preceding section contains the data, plots of the data, statistics and geology for each of the intervals of interest. The last section of this chapter deals with interval velocity measurements' error estimation for each interval and source.

The modeling, results, and interpretation are in chapter 4. The dispersion curves are calculated twice with DWN and LDR. Best Q fits are calculated using least squares. Additionally, included in each interval are plots of: velocity changes from a source frequency to another, overlaid synthetic seismograms calculated from the DWN, dispersion curves of the two methods calculated from the best Q that explains the model, and finally, a plot of the dispersion curves for a homogeneous and heterogeneous medium for the same interval to detect the effects of elastic scattering (if any). The conclusion includes a summary of the results and recommendation for future work. Finally, Appendix B includes more overlaid seismograms for each interval to show the shift caused by attenuation.

Chapter 2

Methodology

We believe that the velocity discrepancies observed in Gypsy field between VSP, Bender, and Sonic log measurements are primarily caused by intrinsic attenuation and elastic scattering. Thus, we will focus our efforts on 1) find a value for the total quality factor (Q_{total}) that would best describe the observed dispersion 2) estimate the contribution of the intrinsic attenuation and elastic scattering to the observed dispersion by modeling 3) calculate the dispersion curves for intervals of interest, and 4) calculate the velocity change from a central source frequency to another.

To implement these four main objectives, we chose four intervals of interest in Gypsy field with different velocity contrasts and rock properties; the first interval consists of mostly shale, the second is mostly sandstone, third is a mixture of both, and fourth is the second and third intervals treated as one formation. The data will be discussed in greater details in the next chapter.

Two methodologies are used to explain the observed velocity discrepancies; the first method is a simple and direct calculation using LDR, and the second method is by modeling intervals of interest using DWN over a range of frequencies (100-10000Hz) and a range of constant Q (10-10000). Approximately, we calculated 325 seismograms for each interval for a combination of frequency and Q values.

In this chapter, we will discuss LDR and the main assumptions made. Moreover, we will explain the theory behind the DWN method and the code used to implement it on our data. Finally, we will discuss the picking method used, estimating elastic scattering contribution to the dispersion, and calculating the velocity changes from a source frequency to another.

2.1 Logarithmic Dispersion Relation (LDR)

Assuming plane waves propagation in a homogeneous medium and using a constant Q, velocity dispersion can be estimated by

$$\frac{V(\omega)}{V(\omega_r)} = 1 + \frac{1}{\pi Q} \ln\left(\frac{\omega}{\omega_r}\right) \tag{2.1}$$

where $V(\omega)$ is the velocity at a specific central frequency, $V(\omega_r)$ is the velocity at a reference frequency, and Q is the quality factor (Aki and Richards, 1980). We chose a reference frequency of 10000 Hz because we have a sonic log velocity measurement at that frequency. Figure 2.1 was calculated using equation 2.1 with a reference velocity of 2.9km/s and a reference frequency of 10000 Hz. Note the velocity change decreases as we increase Q value (medium becoming less attenuative).

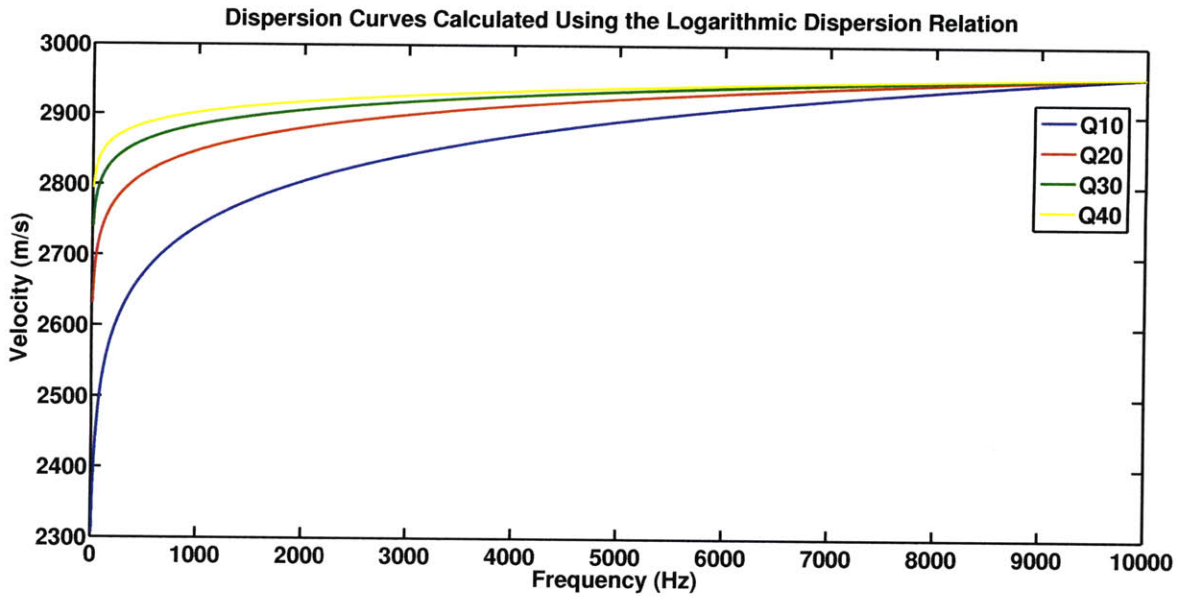

Figure 2.1: Dispersion curves calculated using equation 2.1 showing velocity as a function of frequency for Q values 10,20,30 and 40 and $\omega_r = 10kHz$

Using this relation and least squares, we find the best Q value that would fit the three field velocity measurements with the least error. It is important to note that this value contains the effects of scattering and intrinsic attenuation since we are using the relation to describe the field measurements. Assuming that the dispersion is mainly caused by attenuation due to elastic scattering and intrinsic attenuation, the effective attenuation could be estimated using

$$\frac{1}{Q_{total}} = \frac{1}{Q_{Intrinsic}} + \frac{1}{Q_{Scattering}}. \tag{2.2}$$

2.2 The Discrete Wavenumber Method (DWN)

The DWN was developed by Bouchon and Aki in 1977 to provide an exact calculation and solutions to the complete green's functions for various problems in elastodynamics. In this method, the radiated wavefield is discretized using spatial periodicity of sources followed by calculating the exact solutions to the Green's functions in the complex frequency domain (Bouchon, 2003). Figure 2.2 shows the physical interpretation of the method.

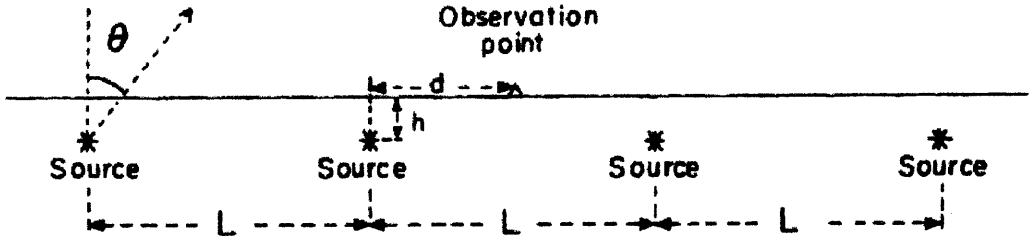

Figure 2.2: Physical interpretation of the DWN method for the 2D case. The source is replaced by infinite number of sources along the horizontal axis at intervals L (Bouchon, 2003).

2.2.1 Method of Computation for the 2D Case

In an infinitely homogeneous model, the steady state radiation from a line source could be described by constant superpositioning of homogeneous and inhomogeneous plane waves (Bouchon, 1979). Consequently, displacement and stress effects can represented by

$$F(x,z;\omega) = \int_{-\infty}^{\infty} f(k,z;\omega)\, e^{-ikx} dk, \tag{2.3}$$

where x is the horizontal axis of the plane wave, z is the vertical axis of the plane wave, and k is the horizontal element of the wavenumber. Next, by adding infinitely many sources spaced equally along the x-axis, equation 2.3 becomes

$$G(x,z;\omega) = \int_{-\infty}^{\infty} f(k,z;\omega)\, e^{-ikx} \sum_{m=-\infty}^{\infty} e^{-ikmL} dk, \tag{2.4}$$

where L is the periodic source interval length, and the summation factor in equation 2.4 can be expressed as

$$\sum_{m=-\infty}^{\infty} e^{-ikmL} = 2\pi \left(\delta \left[kL\right]\right)_{mod2\pi}; \tag{2.5}$$

which reduces to

$$G\left(x, z; \omega\right) = \sum_{n=-\infty}^{\infty} \frac{2\pi}{L} f\left(\frac{2\pi}{L} n, z; \omega\right) e^{-i\frac{2\pi}{L}nx}. \tag{2.6}$$

To calculate the impulse response, we need to find the Fourier transform of equation 2.3 (single source solution) in time domain at distance $x = d$. Let T be the arrival time of the disturbance caused by a source placed at a distance $L - d$ from receiver, and let $0 < t < T$, then, the function

$$f(t) = \int_{-\infty}^{\infty} F\left(x, z; \omega\right) e^{i\omega t} d\omega \tag{2.7}$$

becomes

$$f(t) = \int_{-\infty}^{\infty} e^{i\omega t} d\omega \sum_{n=-\infty}^{n=\infty} \frac{2\pi}{L} f\left(\frac{2\pi}{L} n, z; \omega\right) e^{-i\frac{2\pi}{L}nx}. \tag{2.8}$$

To solve 2.8, we can evaluate the integral using Discrete Fourier Transform (DFT). However, because we added infinite number of sources, using DFT will introduce some aliasing in the time domain solution. To avoid this effect, we need to add a constant negative imaginary part to the frequency (ω_I) so that $e^{\omega_I T} << 1$. This would guarantee that disturbances not part of the time window are attenuated enough for their effect to be negligible. Taking this approach into consideration, the impulse response can be calculated by

$$f\left(t\right) = e^{-\omega_I t} \int_{-\infty}^{\infty} e^{i\omega_R t} d\omega_R \sum_{-n}^{n} \frac{2\pi}{L} f\left(\frac{2\pi}{L} n, z; \omega\right) e^{-i\frac{2\pi}{L}nx}. \tag{2.9}$$

Finally, we use the Fast Fourier Transform (FFT) to evaluate the integral in equation 2.9.

See Bouchon and Aki (1977) and Bouchon (1979, 2003) for more detailed derivations and the 3D case.

2.2.2 Discrete Wavenumber Method Code

The DWN Fortran code used in this thesis was originally developed by Michel Bouchon. The calculations in this code are mainly based on the DWN method and the method of reflectivity and transmissivity matrices. Originally, the source used in the code is the moment tensor derived and calculated from the fault parameters; these parameters are part of the input file and are: azimuth, dip, rake, length and slip of the fault. For the purpose of this thesis, the moment tensor was designated to simulate an explosion source (see appendix A). Additionally, the source wavelet was changed from the Fourier transform of a smooth ramp function to the Fourier transform of a zero-phase Ricker wavelet using the equation

$$f(t) = \left[1 - 2\pi^2 v_0^2 t^2\right] e^{-\pi^2 v_0^2 t^2} \tag{2.10}$$

with the peak centered at $t = 0$ (Stein and Wysession, 2003). The input file consists of 23 parameters; these describe the velocity model, quality factors, source(s) and receiver(s) location and source central frequency. The output file consists of three columns; index of the seismogram, time, and displacement or velocity, respectively. Finally, anelastic attenuation effects are calculated by

$$\frac{\omega}{c\left(\omega\right)} = \frac{\omega}{c_\infty} + H\left[\alpha\left(\omega\right)\right] \tag{2.11}$$

and

$$aq \int_{\infty}^{0} \frac{e^{i\omega t}}{1+at} dt \approx -q\left[\gamma + log\left(\frac{\omega}{a}\right) - \frac{i\pi}{2}\right] e^{-i\frac{\omega}{a}}, \tag{2.12}$$

where $c(\omega)$is the velocity, $\alpha(\omega)$is the attenuation factor, H is the Hilbert transform, a is the fundamental frequency, and γ is Euler's constant (Aki and Richards, 1980).

2.2.3 General algorithm for the DWN code

Figure 2.3shows a diagram shows a simplified algorithm that broadly describes the steps used in the code to calculate the synthetic seismograms:

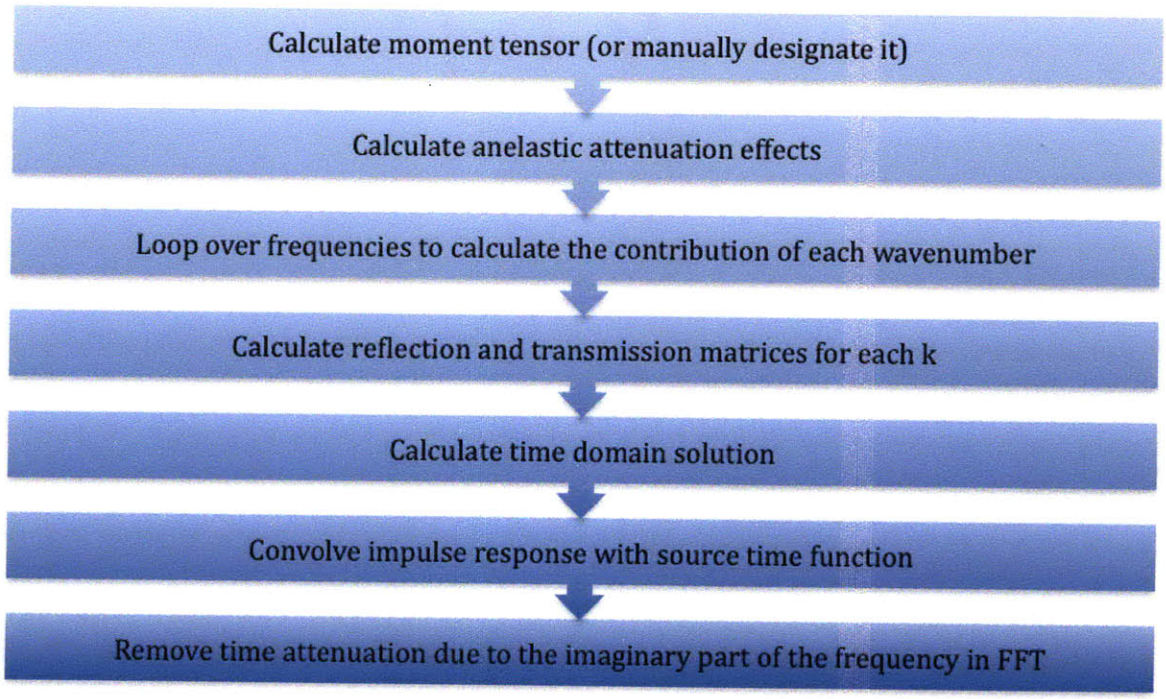

Figure 2.3: DWN code flow diagram

2.2.4 Modeling Velocity Dispersion Using the DWN method

The second approach is modeling velocity dispersion using the DWN method. Unlike the first approach, where it is assumed that the model is homogeneous, we can approximate how much of the velocity dispersion is due to intrinsic attenuation and how much is due to elastic scattering. Figure 2.4 shows a typical design used in modeling the four intervals. The input velocity models are padded with a thick 1000m layer from the top with the same properties as the first layer, and another 1000m thick layer from the bottom with same properties

as the last layer, to simulate perfectly matched layer effect (PML) similar to that in finite differencing. The offset between the source and receiver is zero.

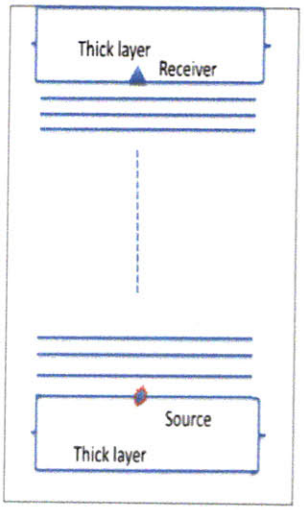

Figure 2.4: Typical design used in modeling Gypsy intervals in this thesis

For each interval, we generate synthetic seismograms for Q values [10, 15, 20, 25, 30, 40, 45, 50, 55, 60, 70, 80, 90, 100, 200, 500, 10000] and for each Q value, we generate another set of seismograms with central frequencies [100, 200, 300, 400, 500, 700, 1000, 2000, 2500, 5000, 7500, 10000]. Next, we pick the first arrival times for these synthetic seismograms. Since we modified the code to use a Ricker wavelet with its peak at $t = 0$, we consistently picked the peak as the first arrival. Using these travel times, we calculate the velocities and generate dispersion curves as well as calculate the velocity changes from a source frequency to another.

For vertical propagation, the higher the velocity contrast, the more weight scattering effects will have on velocity dispersion. We use two approaches to estimate the effects of scattering on velocities (if any). First, we start by modeling the intervals of interest with medium velocities obtained from FWS logs with a very high constant Q value (non-attenuative medium) over a range of central frequencies (100hz to 10000hz). If we observe little or no difference in velocities, we conclude that the scattering component is very small and the dispersion is primarily caused by intrinsic attenuation. The second approach is

we model the same interval twice with a constant Q over the same range of frequencies; once with a constant interval velocity calculated from the average slowness, and another with varying velocity. The difference between the two picked arrival times is assumed to be caused by scattering.

2.3 Summary of The Work Flow Used for Each Interval to Estimate Q

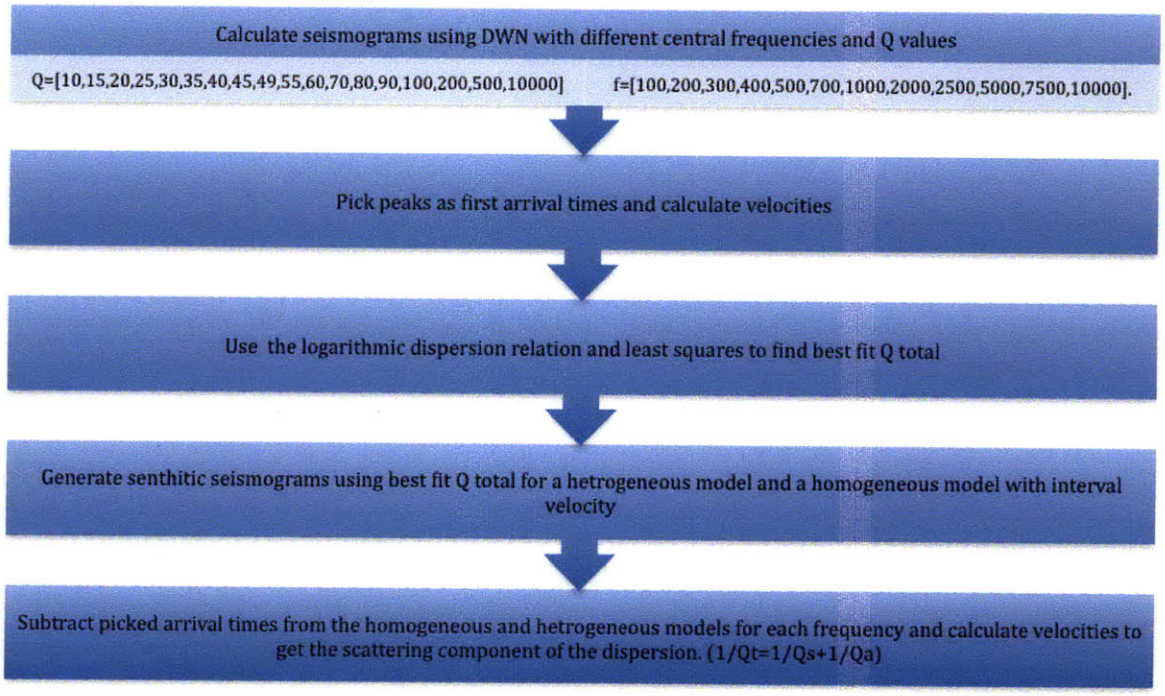

Figure 2.5: Workflow used to estimate $Q_{intrinsic}$and $Q_{scattering}$

Chapter 3

Gypsy Site Data

Gypsy test site is located in central Oklahoma in Pawnee County. It was founded by British Petroleum Exploration Inc and later donated to the University of Oklahoma in 1992. The main objective of this project was to develop a set of geophysical tools and techniques for integrated reservoir characterization (Turpening et al., 1992). Aggregate cost of the acquired data was estimated to be $2.5 million (Doyle et al., 1992). We consider this site excellent for the purpose of studying velocity dispersion because of the following reasons: 1) Wide range of geologic and geophysical data acquired, 2) it is highly heterogeneous, and 3) the site is water-saturated and thereby reducing the complications of multi-phase fluid systems (Burns and Martin, 1993).

The project was implemented in three stages (Doyle et al., 1992):

1. Sampling the geologic units of an outcrop exposed by a road-cut with particular focus on the Gypsy sandstone interval to develop an extensive distribution of reservoir properties.

2. Surface seismic and borehole data acquisition. A 3-D surface seismic survey was carried out and 5 wells were drilled in the pattern shown in figure 1. The types of data collected from the wells are: gamma, porosity, density, FWS and 'bender' logs. Additionally, a cross-well survey was obtained between well 5-7 and 1-7. Vertical Seismic Profiling

(VSP) survey was also obtained for wells 5-7 and 1-7.

3. Reservoir quality characterization through well testing.

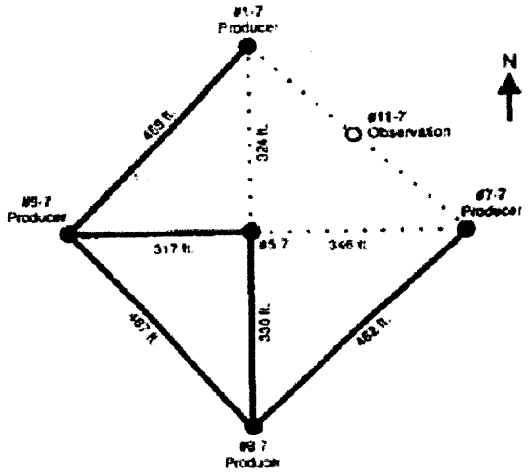

Figure 3.1: Gypsy site wells. We will be using data from well 5-7 for the purpose of this thesis (Burns and Martin, 1993)

For the purpose of this thesis, we will be using data from well 5-7. We will be using gamma, density, VSP, Bender, and FWS logs to measure and model the observed velocity dispersion. In this chapter, we will generally discuss the geologic context of Gypsy site, data acquisition, and data for the intervals of the area of interest.

3.1 Geologic Context of the Gypsy Site

The "Gypsy Sandstone" interval top is at a depth of around 270m and on average is 35m thick. For this thesis, we identified three intervals of interest that include the Gypsy sandstone interval (237m to 322m). The data used to describe the geology in literature uses 22 1" cores from the exposed outcrop located 15 miles southeast of Gypsy site on highway-64, and the logs and cores acquired from the wells. A detailed discussion of the depositional environments was done by Parra et al. (1994) and Doyle et al. (1992).

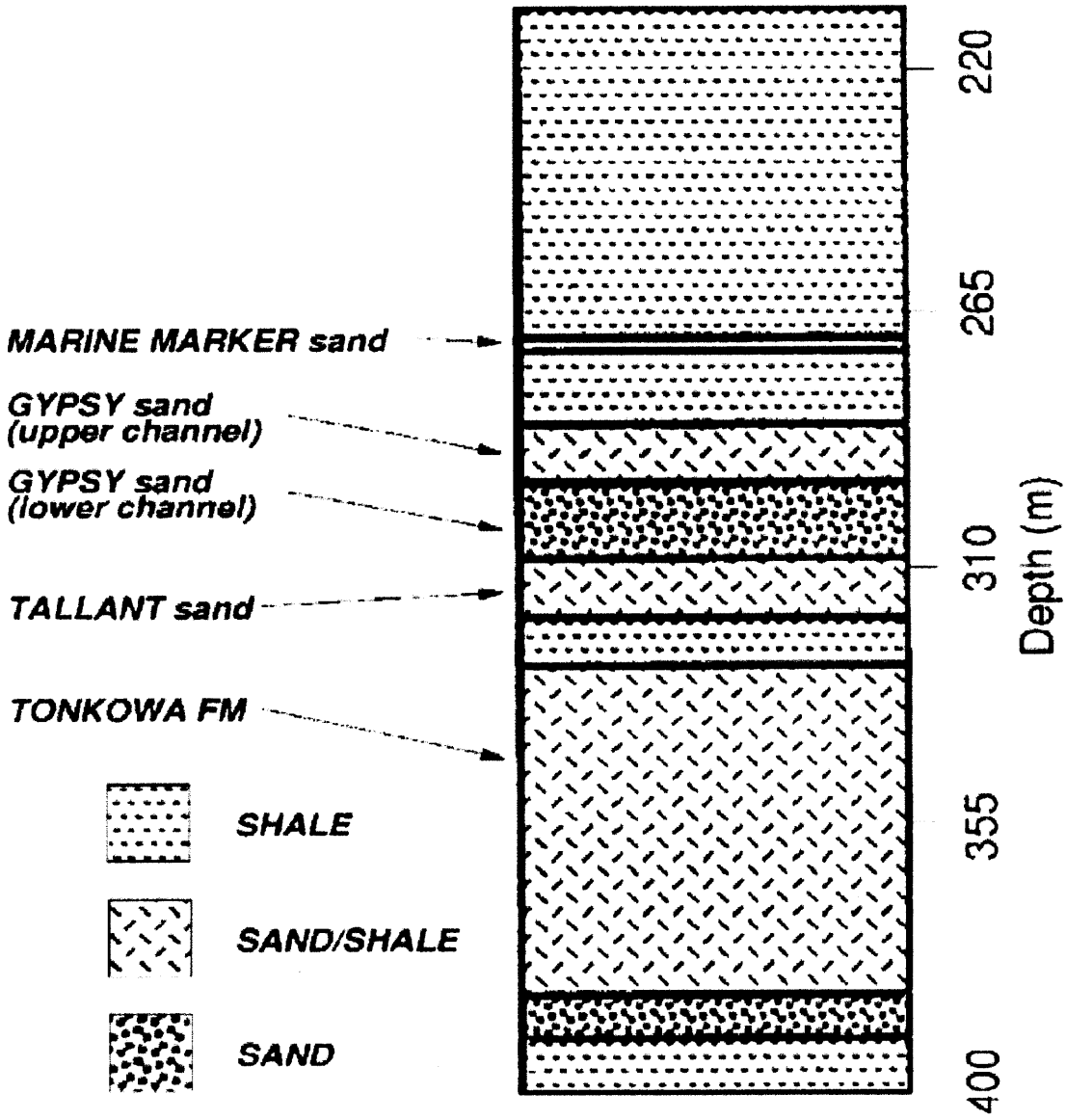

Figure 3.2: Regional lithology of the intervals of interest (Liao and McMechan, 1997)

Essentially, the interval of interest is part of two formations; the upper part is the lowermost part of the Virgilian age Vamoosa formation and the bottom part is the uppermost section of the Missourian age Tallant formation. The Gypsy interval was deposited over an unconformity and consists of stacked channel sandstones, siltstones and mudstones (Parra et al., 1992). It is surrounded by marine flooding surfaces from the top and bottom. The

top contact above the Gypsy interval is mainly composed of marine shale while the bottom contact consists of low porosity siltstone and mudstone. Figure 2.1 shows the regional lithology of the intervals of interest adapted from Liao and McMechan (1997). Figures 3.3 and 3.4 include the entire field data measured from well 5-7 for the area of interest that is used in this thesis. In the third section of this chapter, we will break it into three intervals and discuss each of them.

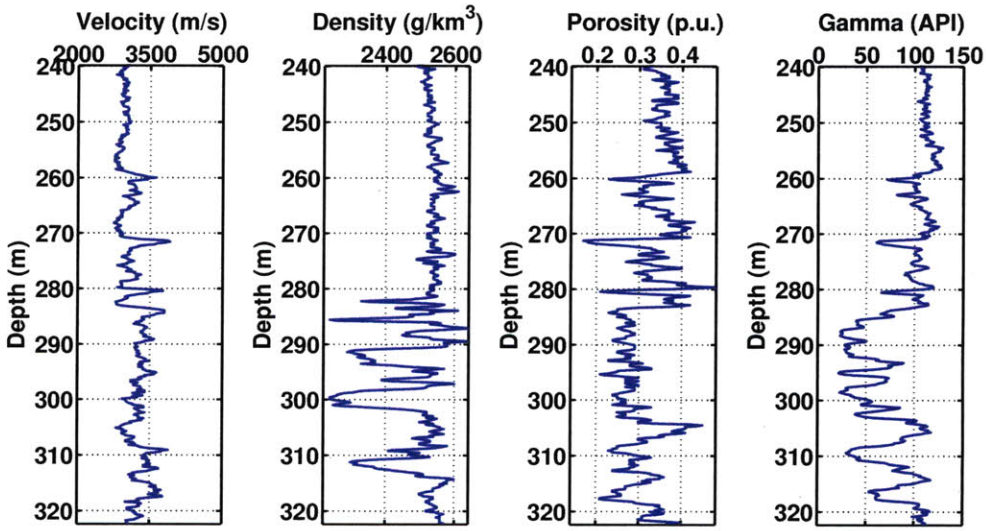

Figure 3.3: Well logs from well 5-7 covering the areas of interest (all four intervals)

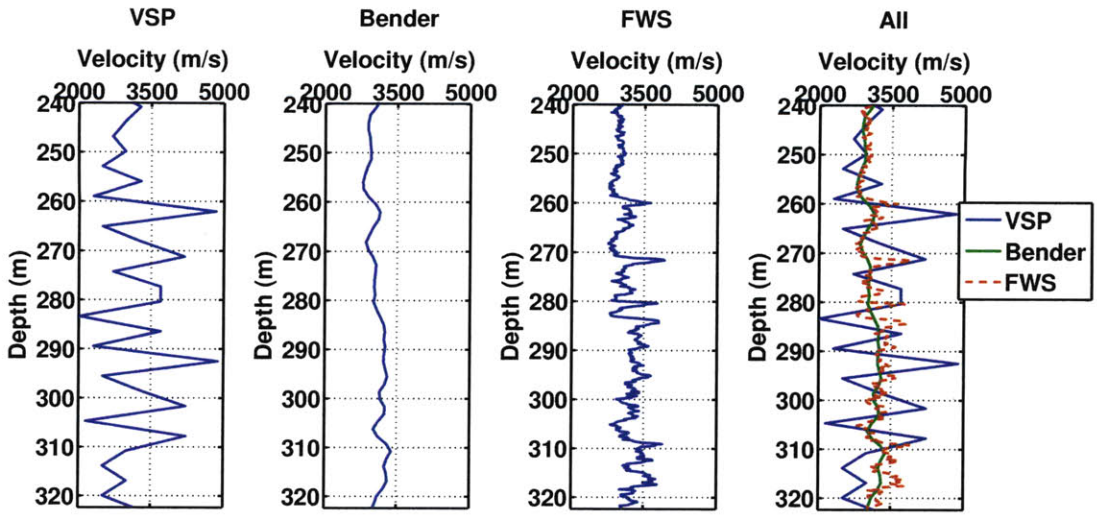

Figure 3.4: VSP, Bender, and FWS velocity logs covering all areas of interest

3.2 Data Acquisition

We are interested in modeling and explaining the velocity discrepancies observed from field borehole measurements. Thus, we will be using VSP, bender and FWS logs to demonstrate and model the dispersion. In this section, we will discuss the technical details and geometry for each source. We used NER report (1993) to obtain these technical details.

3.2.1 Vertical Seismic Profile (VSP)

The VSP data was acquired by Atlas Wireline using an ARIS source located around 52m away from the wellhead. The recording sampling rate was 1 ms and the spatial sampling rate was 3.02m. Receivers were placed north and south of the well. The central frequency for the compressional wave (P-wave) was between 50Hz and 100Hz. Due to the coarse spatial sampling rates, the calculated interval velocities varied significantly enough to limit our use of these measurements. Additionally, we don't have access to the VSP waveforms that we would like to use to get a better estimate of the central frequency; however, we estimated the central frequency by counting the events and dividing them by time from a hard copy of

the waveforms; we got a central frequency of 100Hz.

3.2.2 Bender

The 'bender' log is a low frequency, long offset compared with FWS. The data were collected by NER (Burns et al., 1993). Figure 3.5 shows the two array configurations used. The first array uses a source depth interval of 1.5m with a pulse that is half the cycle of a 1000Hz sine wave. The second array uses a source depth interval of 1.5m with a pulse that is half the cycle of a 2000Hz sine wave. We will be using the logs from the first array configuration. We also don't have the waveform data so we used the same approach as VSP to estimate the central frequency. We used a hard copy of the stacked seismograms (figure 3.6) and got a central frequency of 1000 Hz.

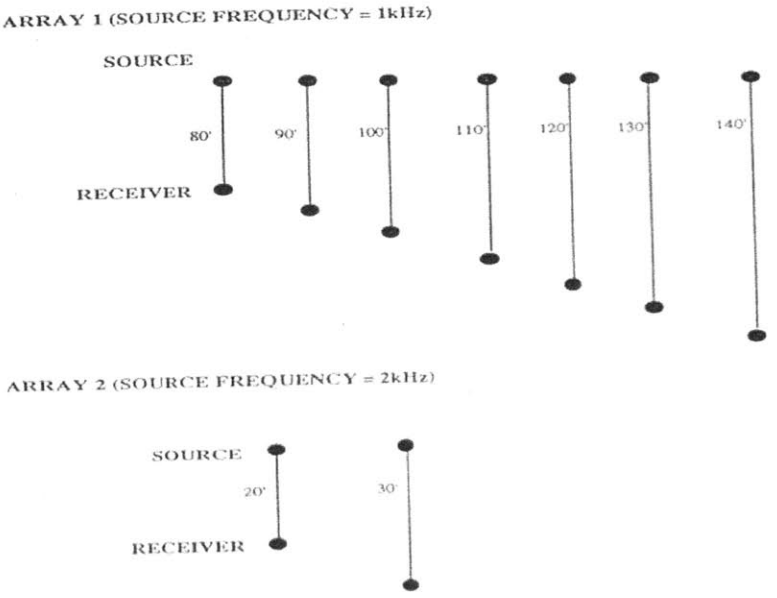

Figure 3.5: Bender Geometry (Burns and Martin, 1993)

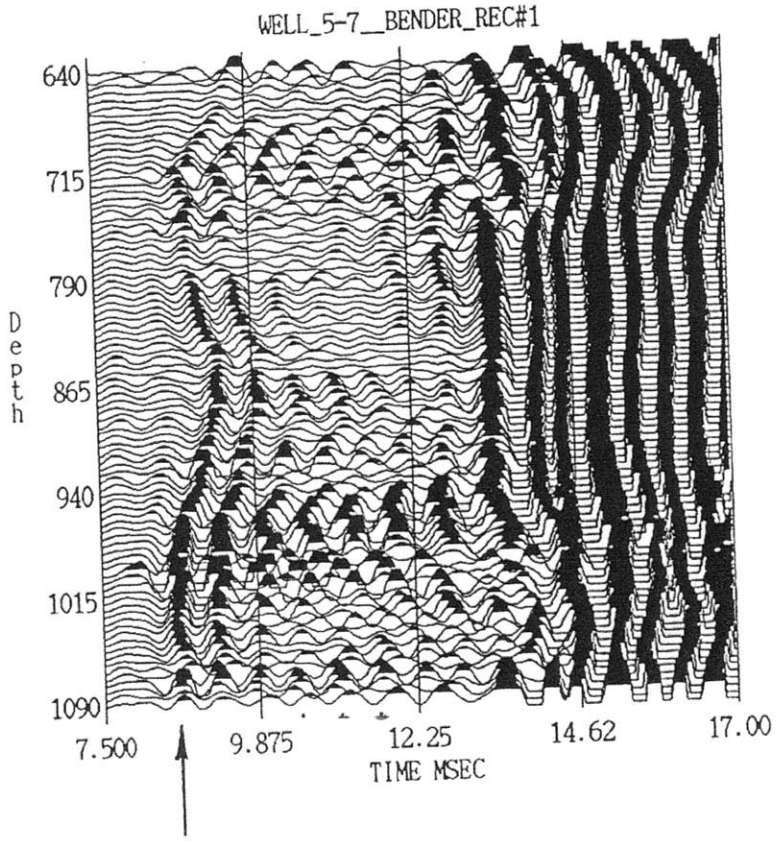

Figure 3.6: Bender waveforms from a receiver located 24.5m from the source. The arrow points at the comperssional waves first arrival. Arrivals after around 14ms are tube waves (Burns and Martin, 1993)

3.2.3 Full-wave Sonic (FWS)

FWS data, also referred to as Full Waveform Acoustic Log (FWS), was acquired by Schlumberger using SDT-A tool. The tool has 8-receiver monopole array equally spaced at 0.1542m with the first receiver located 2.44m away from the source. Data was processed using the semblance method to produce slowness values every 0.1542m where the values are the average of slowness across the 1.067m receiver aperture. The central frequency is assumed to be 10000Hz. Like it is the case with the VSP and Bender, we only have access to a hard copy of the waveforms (figure 3.7). Manually counting the events and dividing the number of events over time leads to a frequency range of 7000Hz to 15000Hz. We will consider this

in our analysis in the results chapter of this thesis.

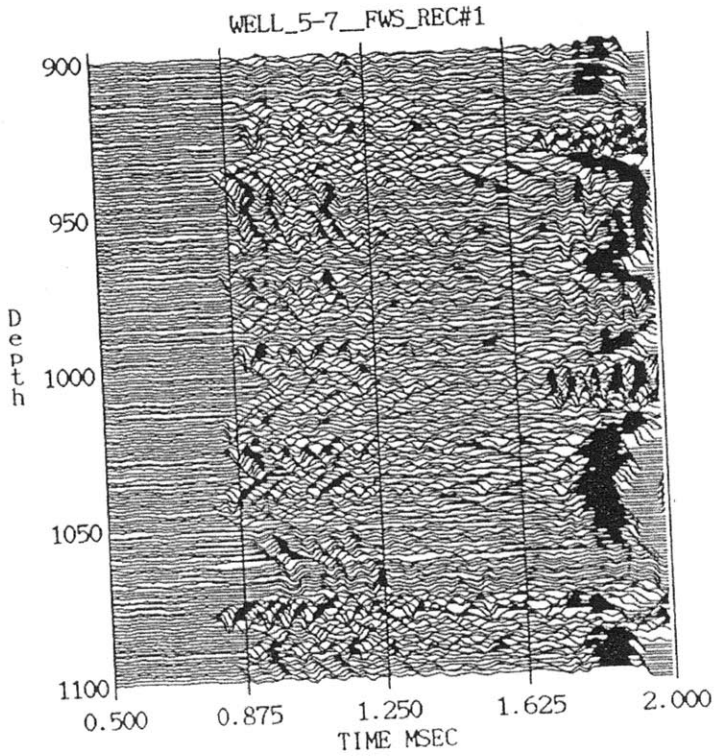

Figure 3.7: FWS waveforms (Burns and Martin, 1993)

3.3 Intervals of Interest

We have identified four intervals of interest with varying rock properties. The 'Gypsy Sandstone' is among them. The second and third intervals are consecutive, thus, we will analyze and model each interval separately and combined as well; we want to know which approach would lead to a better estimate of Q and whether these two intervals are better treated as one or separate when estimating the observed dispersion. The average interval thickness is 20m. We will use the FWS log as the initial velocity model when modeling the data (wave propagation). Velocities were calculated from the slowness by

$$V = \frac{1}{Slowness} \tag{3.1}$$

and the interval velocity is the calculated the same way by taking the inverse of the average slowness. The calculated time essentially is dividing distance over velocity for each measurement and the calculated interval velocity is obtained by dividing the total distance over the total travel time.

3.3.1 Interval One: 239.1m to 259.5m

This interval is predominantly shale. It lies above Gypsy Sandstone and is part of the Vamoosa formation. Changes in porosity, density and velocities are very small (figure 3.8). Thus, we expect that the observed dispersion to be mainly caused by intrinsic attenuation. The change in velocity between FWS and VSP is 80.2m/s and between FWS and Bender is 37.1m/d. Table 3.1 contains a summary of the field data and statistics (calculated from FWS). Figures 3.8,3.4, and 3.10 show plots of the field data for this interval.

Begin	239.1	m
End	259.5	m
Thickness	20.5	m
Maximum Velocity	3177.7	m/s
Minimum Velocity	2771.9	m/s
Average Velocity	2958.4	m/s
Calculated Time	0.006961	s
Calculated Interval Velocity	2955.6	m/s
Average Density	2.502	g/km^3
Maximum Gamma	129.1	API
Minimum Gamma	93.1	API
Average Gamma	113.2	API
FWS Interval Velocity	2955.6	m/s
Bender Interval Velocity	2918.5	m/s
VSP Interval Velocity	2875.5	m/s

Table 3.1: Interval one field data and statistics

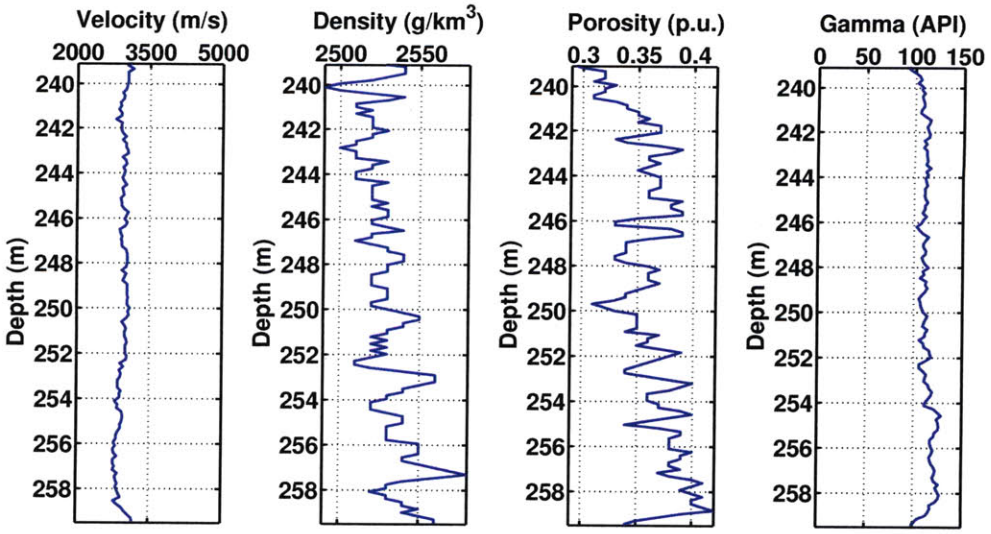

Figure 3.8: Interval one well logs. The velocity log is from FWS. This interval is predominantly shale and largely homogeneous as evident from the Gamma log

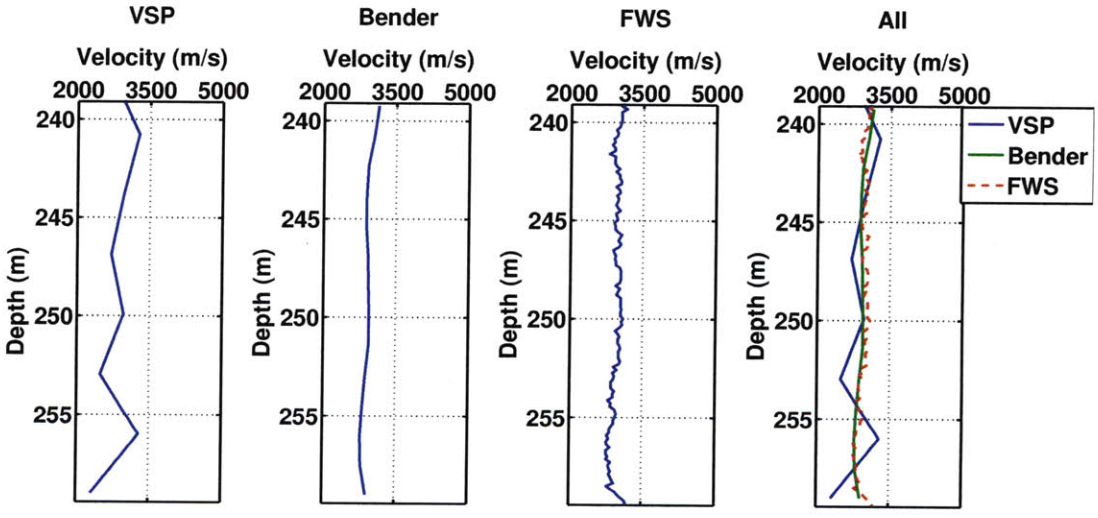

Figure 3.9: Interval one velocities from VSP, Bender and FWS.

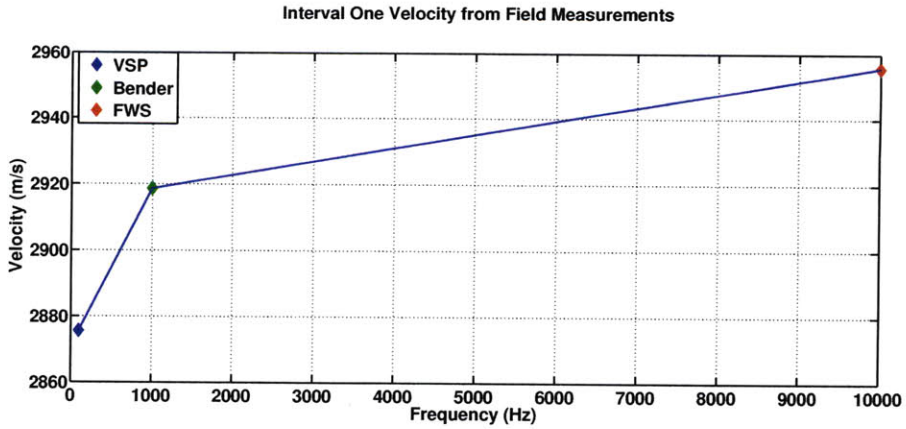

Figure 3.10: Interval one interval velocities from VSP, Bender and FWS estimated from slowness.

3.3.2 Interval Two: 281.6m to 304.6m

This interval is predominantly sandstone and siltstone. It is part of the Tallant formation. Strong changes in density are due to thin layers part of the stacked channels in the Gypsy sandstone. The velocity change between FWS and VSP is 139.9m/s and between FWS and Bender is 66.8m/s. Table 1 contains a summary of the field data and statistics (calculated from FWS). Figures 3.11, 3.12, and 3.13 show plots of the field data for this interval. Table 3.2 contains a summary of the field data and statistics.

Begin	281.6	m
End	304.6	m
Thickness	23.2	m
Maximum Velocity	3804.3	m/s
Minimum Velocity	2801.7	m/s
Average Velocity	3292.8	m/s
Calculated Time	0.007	s
Calculated Interval Velocity	3305.3	m/s
Average Density	2.4526	g/km^3
Maximum Gamma	114.4	API
Minimum Gamma	22.3	API
Average Gamma	56.7	API
FWS Interval Velocity	3281.5	m/s
Bender Interval Velocity	3214.7	m/s
VSP Interval Velocity	3142.3	m/s

Table 3.2: Interval two field data and statistics

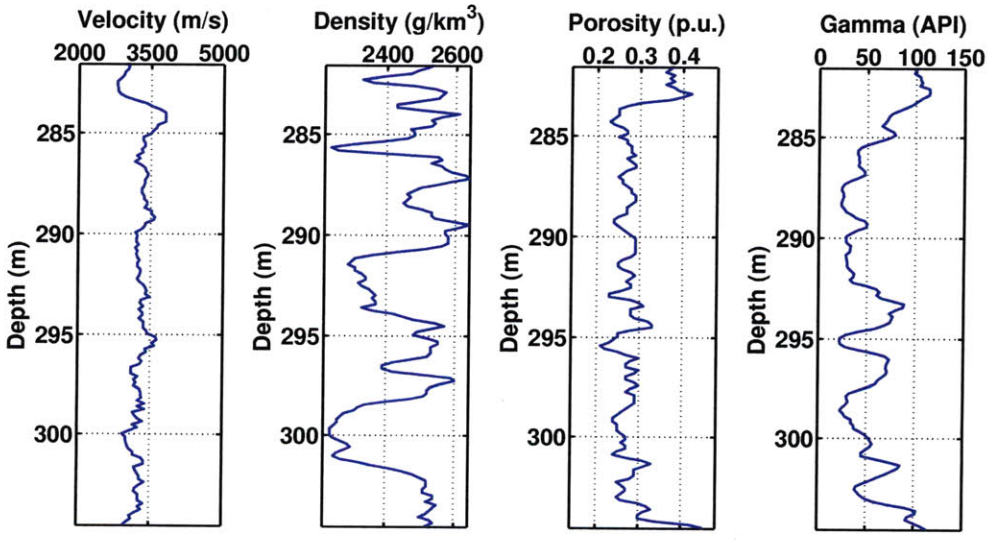

Figure 3.11: Interval two well logs. The velocity log is from FWS.

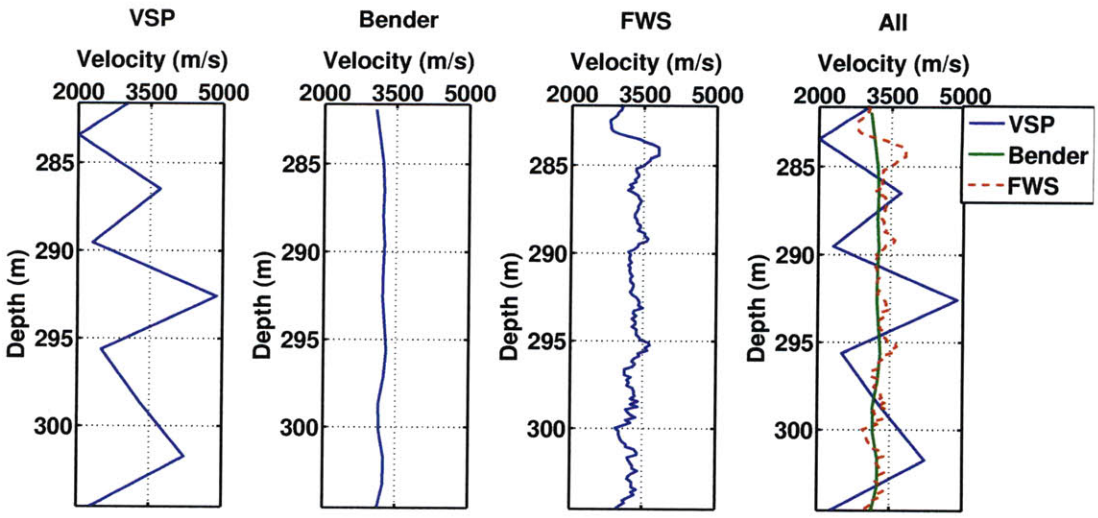

Figure 3.12: Interval two velocities from VSP, Bender and FWS.

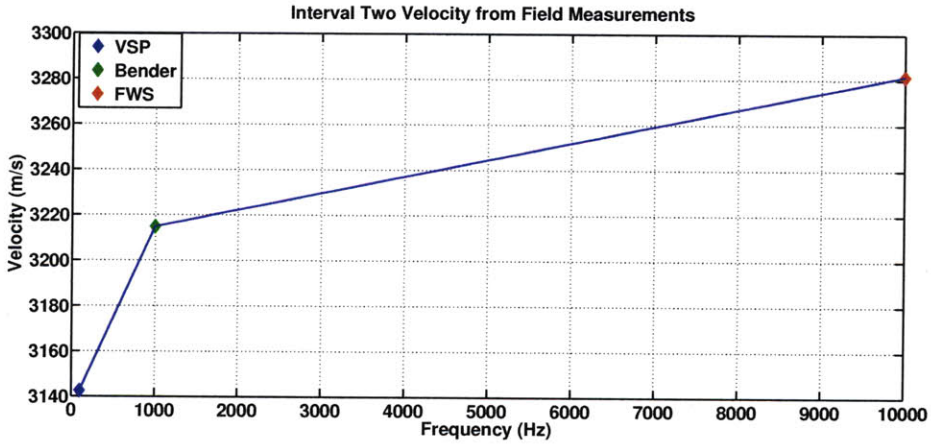

Figure 3.13: Interval two interval velocities from VSP, Bender and FWS estimated from slowness.

3.3.3 Interval Three: 304.7m to 322.4m

This interval is a mix of sandstone and shale. It is part of the Tallant formation. The velocity change between FWS and VSP is 167.6m/s and between FWS and Bender is 89.9m/s. Table 3.3 contains a summary of the field data and statistics. Figures 3.14, 3.15, and 3.16show plots of the field data for this interval.

Begin	304.7	m
End	322.4	m
Thickness	17.9	m
Maximum Velocity	3889.2	m/s
Minimum Velocity	2816.7	m/s
Average Velocity	3309.7	m/s
Calculated Time	0.0054	s
Calculated Interval Velocity	3327.1	m/s
Average Density	2.5102	g/km^3
Maximum Gamma	117.63	API
Minimum Gamma	30.25	API
Average Gamma	84.9337	API
FWS Interval Velocity	3292	m/s
Bender Interval Velocity	3202.2	m/s
VSP Interval Velocity	3124.5	m/s

Table 3.3: Interval three field data and statistics

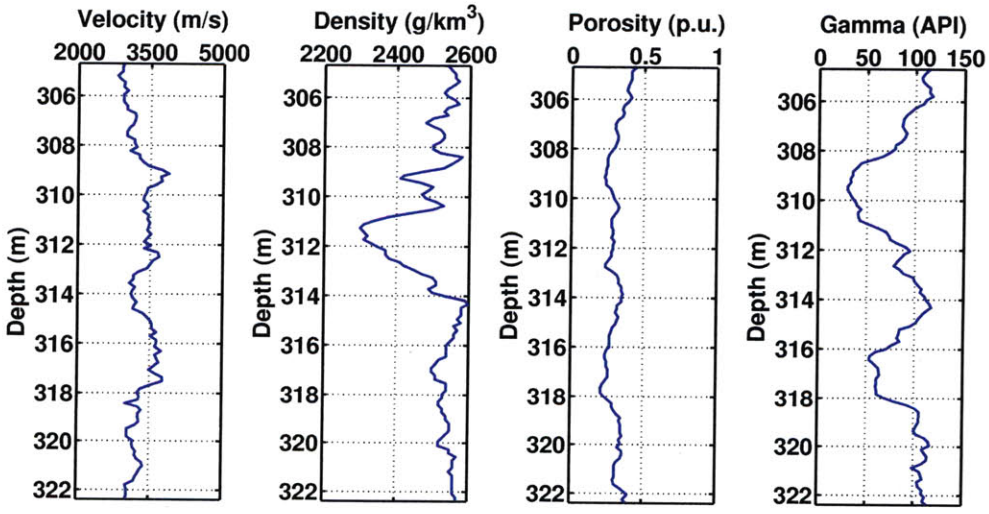

Figure 3.14: Interval three well logs. The velocity log is from FWS.

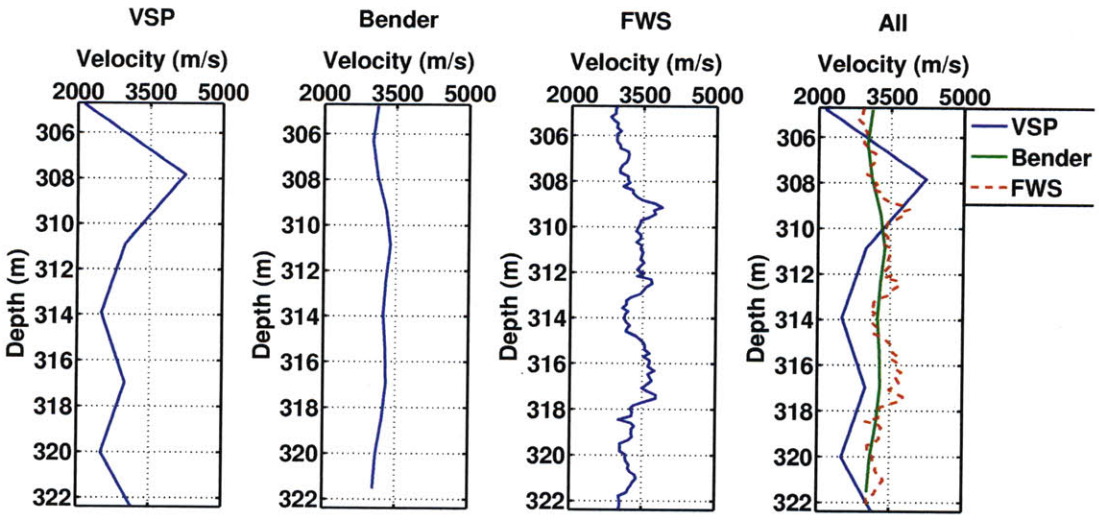

Figure 3.15: Interval three velocities from VSP, Bender and FWS.

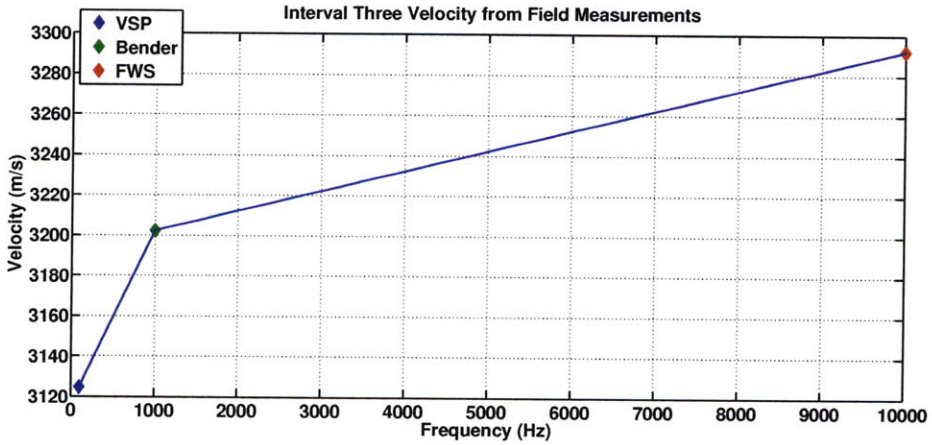

Figure 3.16: Interval three interval velocities from VSP, Bender and FWS estimated from slowness.

3.3.4 Interval Four: 281.6m to 322.4m

This interval treats the second and third interval as one formation. It is part of the Tallant formation. The travel distance in this interval is double and highly heterogeneous, thus, we expect elastic scattering effects to be part of the velocity dispersion. The velocity difference between FWS and VSP is 162m and between FWS and Bender is 73.3m. Table 4 contains a summary of the field data and statistics. Figures 3.17, 3.18, and 3.19 show plots of the field

data for this interval. Table contains a summary of the field data and statistics.

Begin	281.6	m
End	3224	m
Thickness	41	m
Maximum Velocity	3889.2	m/s
Minimum Velocity	2801.7	m/s
Average Velocity	3300.2	m/s
Calculated Time	0.0124	s
Calculated Interval Velocity	3299.7	m/s
Average Density	2.4777	g/km^3
Maximum Gamma	117.63	API
Minimum Gamma	22.33	API
Average Gamma	68.9718	API
FWS Interval Velocity	3286.1	m/s
Bender Interval Velocity	3212.8	m/s
VSP Interval Velocity	3124.1	m/s

Table 3.4: Interval four field data and statistics

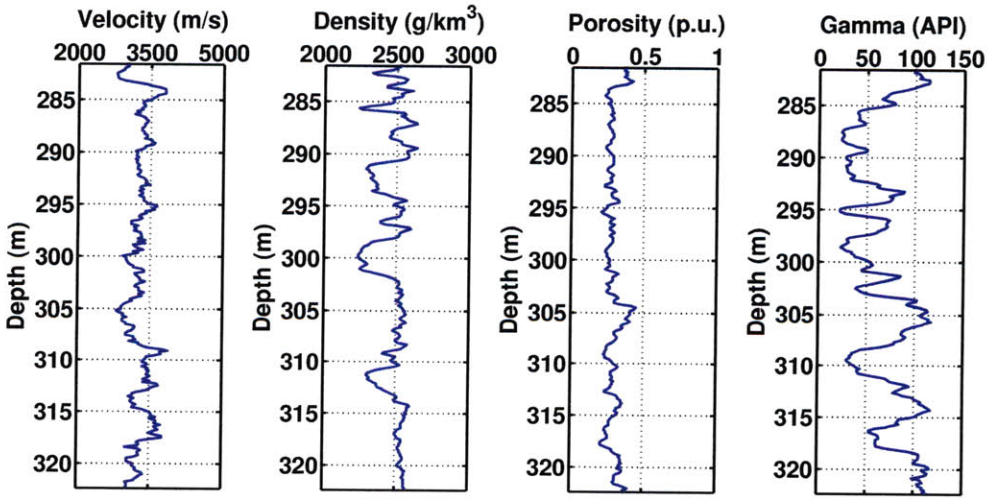

Figure 3.17: Well logs for interval four. The velocity log is from FWS.

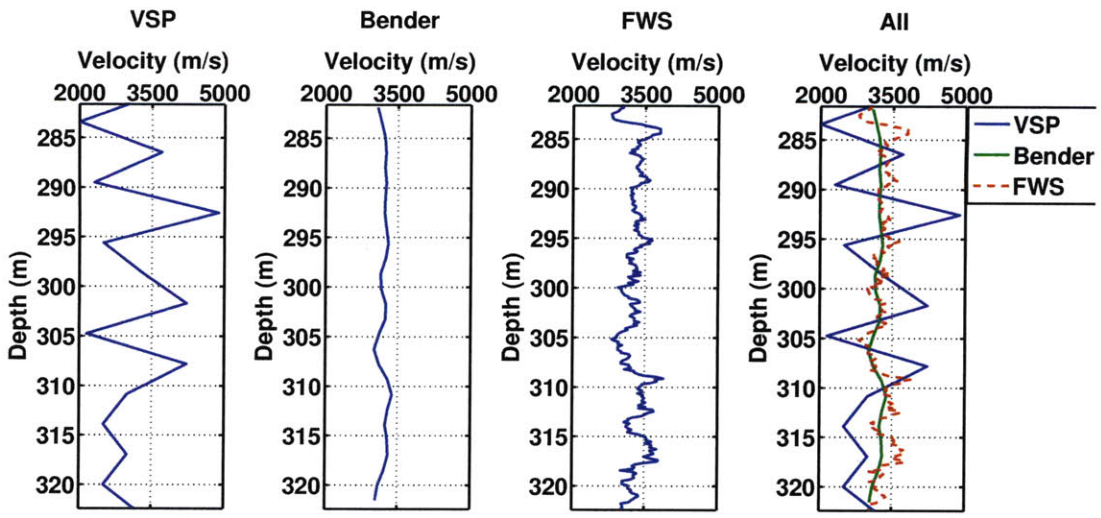

Figure 3.18: Interval four velocities from VSP, Bender and FWS.

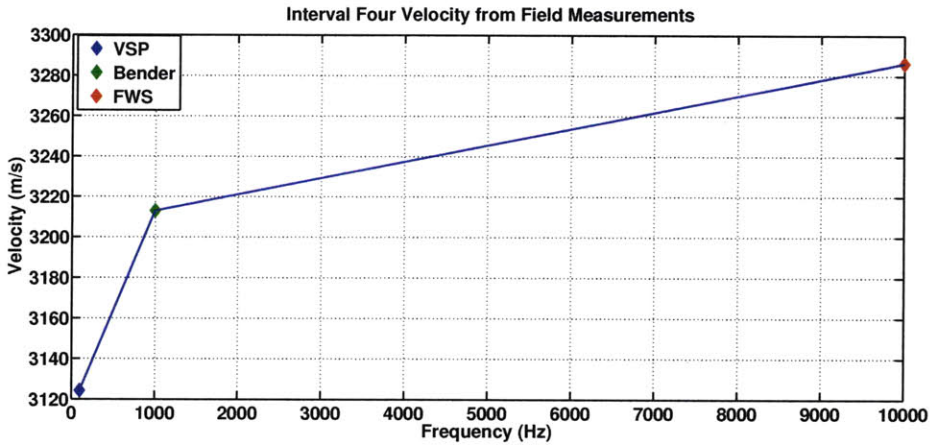

Figure 3.19: Interval four interval velocities from VSP, Bender and FWS estimated from slowness..

3.4 Velocity Error Estimation

The interval velocities from each of the three source frequencies were calculated by averaging the slownesses for each interval. Essentially, the values we get are for a homogeneous medium obtained from a heterogeneous medium. Consequently, some error will be introduced and needs to be accounted for when finding the best Q that would explain the observed dispersion. We use the following relation from Brown and Seifert (1994) to estimate these errors:

$$\triangle V = \frac{\triangle T}{T} * V_m, \tag{3.2}$$

where V_m is the measured velocity, $\triangle V$ is the velocity error, $\triangle T$ is the timing error, and T is the total travel time. We estimated the timing error by assuming a $\frac{1}{20}\lambda$ picking accuracy. The error calculations in table 3.5 were made using table 3.2. For each interval, we calculated the moving error and took its average as the final error value. As mentioned earlier in this thesis, the VSP sampling is very coarse and thus we had to base our calculations of the error on long measurement intervals. We chose a measurement interval of 42.7m which is bigger than the intervals of interest. Consequently, we calculated the error using all acquired measurements (120m to 335m). We obtained a final error value of $\pm$76m/s. Figures 3.20,3.21,3.22, and 3.23show the calculated errors for each interval for FWS and Bender. Figure 3.24 shows the error for VSP.

Interval	Source	ω (Hz)	$\triangle T$(s)	Measurement Interval (m)	$\triangle V_{average}$(m/s)
One	Bender	1000	$5 * 10^{-5}$	16	24
	FWS	10000	$5 * 10^{-6}$	2.1	19
Two	Bender	1000	$5 * 10^{-5}$	16	28
	FWS	10000	$5 * 10^{-6}$	2.1	23
Three	Bender	1000	$5 * 10^{-5}$	16	27
	FWS	10000	$5 * 10^{-6}$	2.1	25
Four	Bender	1000	$5 * 10^{-5}$	16	27
	FWS	10000	$5 * 10^{-6}$	2.1	24

Table 3.5: Velocity error estimation

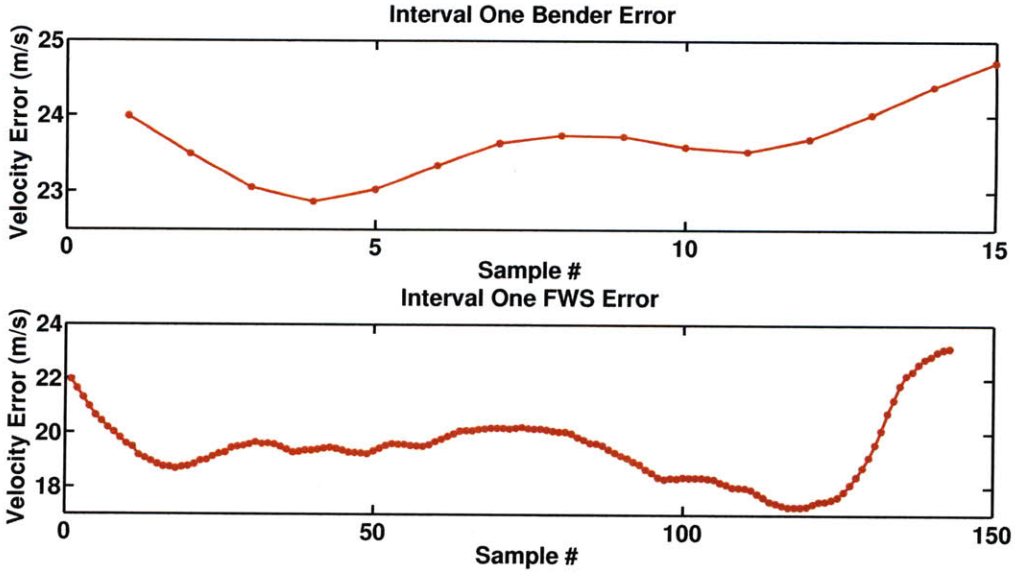

Figure 3.20: Interval One Velocity Error

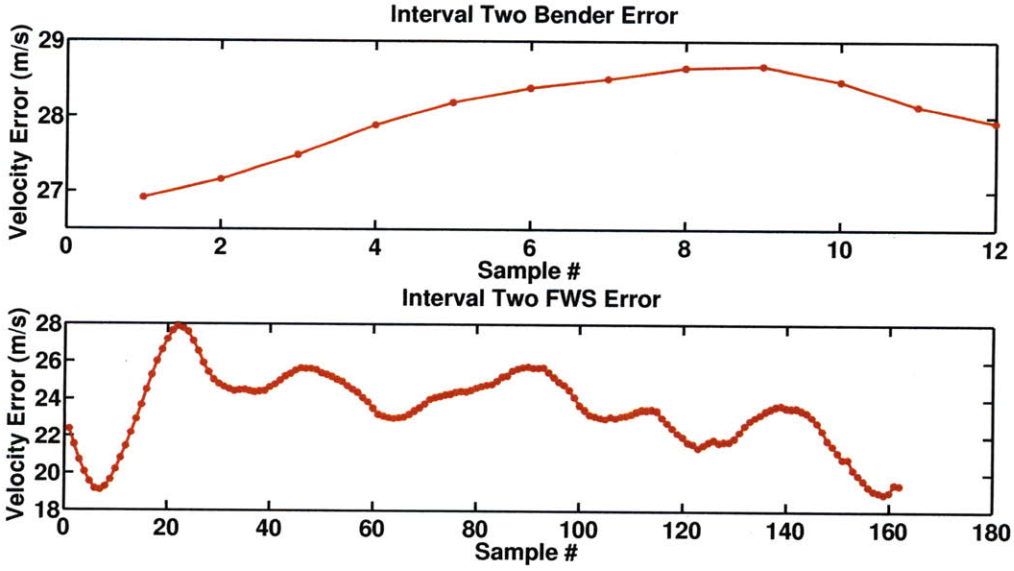

Figure 3.21: Interval Two Velocity Error

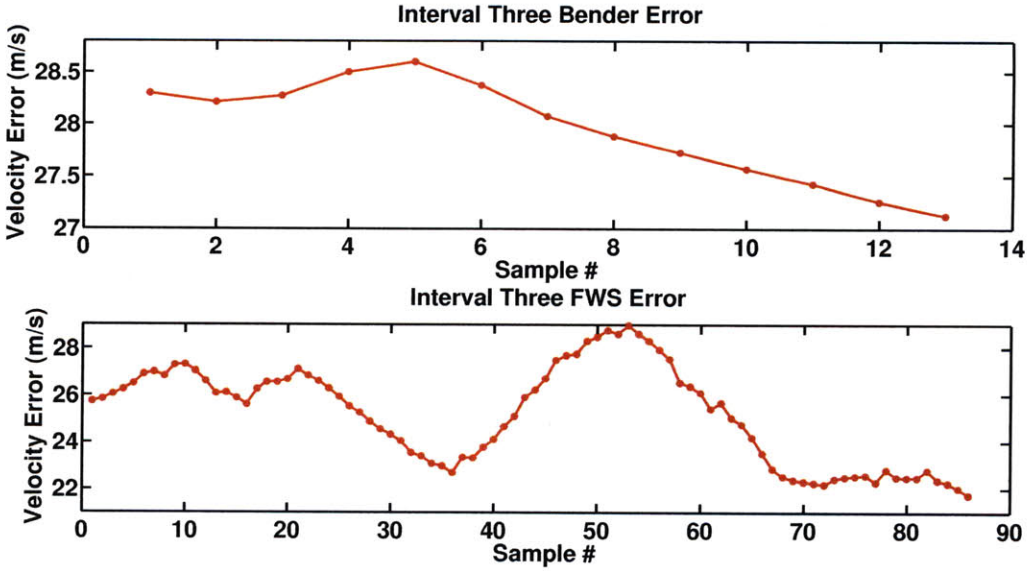

Figure 3.22: Interval Three Velocity Error

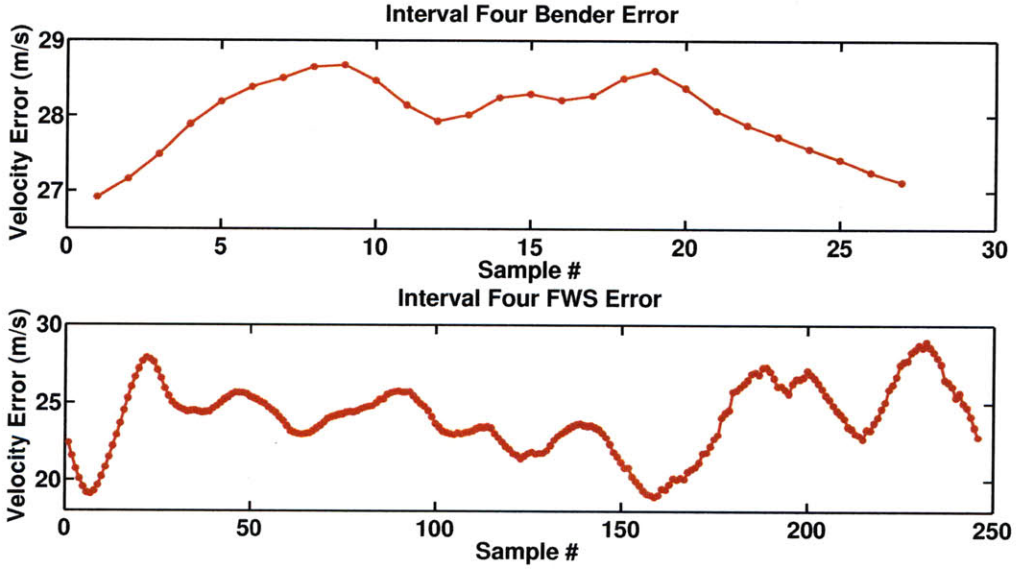

Figure 3.23: Interval Four Velocity Error

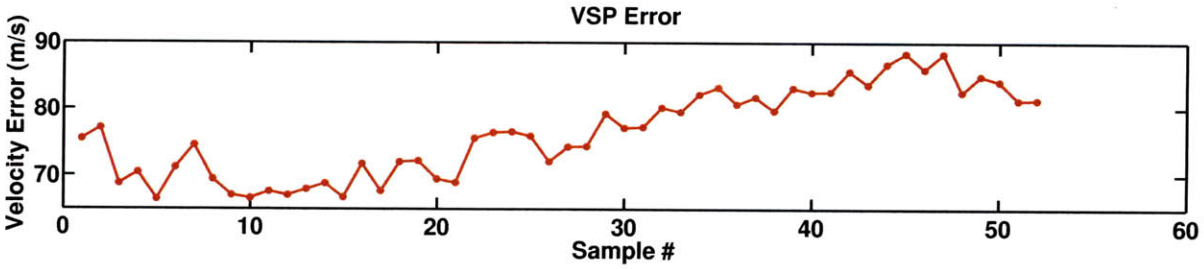

Figure 3.24: Intervals Combined VSP Velocity Error

Chapter 4

Results and Interpretation

Elastic scattering and intrinsic attenuation are assumed to be the main mechanisms responsible for much of the observed dispersion. We take two approaches to model the velocity dispersion observed at Gypsy. First, we use LDR to calculate the dispersion curves and find the best Q that would explain the field data. Second, we use the discrete wavenumber method to do one-way wave propagation through the intervals of interest with different central frequencies and Q values. Jointly, these two approaches provide a good estimate of the dispersion observed and its components.

The LDR approach is simple and direct and provides a good starting point for investigating velocity dispersion. We use equation 1 in the methodology chapter to produce the dispersion curves for each interval. Essentially, this method could be viewed as curve fitting by varying the Q values and/or reference frequency. We chose a reference frequency of 10000 Hz because we have field measurement at that frequency. While the relation assumes that plane waves propagate in an infinitely homogeneous medium, the Q that best fits the field data points contains both components of velocity dispersion: elastic scattering and intrinsic attenuation. This is true because we are changing the Q value to find the best fit to the field data, which contains these effects in addition to measurement errors and volume differences.

In the following sections, we will show the results and best Q that describes the field

data for each interval; we will address the measurement errors by providing a range of other possible Qs. We will discuss some modeling details that are more relevant in this chapter and not covered in the methodology chapter. Our observations are consistent for the four intervals we modeled; to avoid repetition, we will discuss the first interval in detail and limit the other three intervals subsections to results.

4.1 Interval One

This interval is largely homogeneous (shale) and velocity is nearly constant. Thus, we expect intrinsic attenuation to be the primary reason for the observed dispersion. We start by calculating the dispersion curves for a Q range between 10 and 10000 using LDR and DWN method (modeling). Figure 4.1 show the results from the direct LDR method. As Q increases, the velocity difference decreases. Using a Q of 10000 is essentially assuming no attenuation and thus calculated velocities are the same for all frequencies. Moreover, using Q>30, the dispersion significantly decreases.

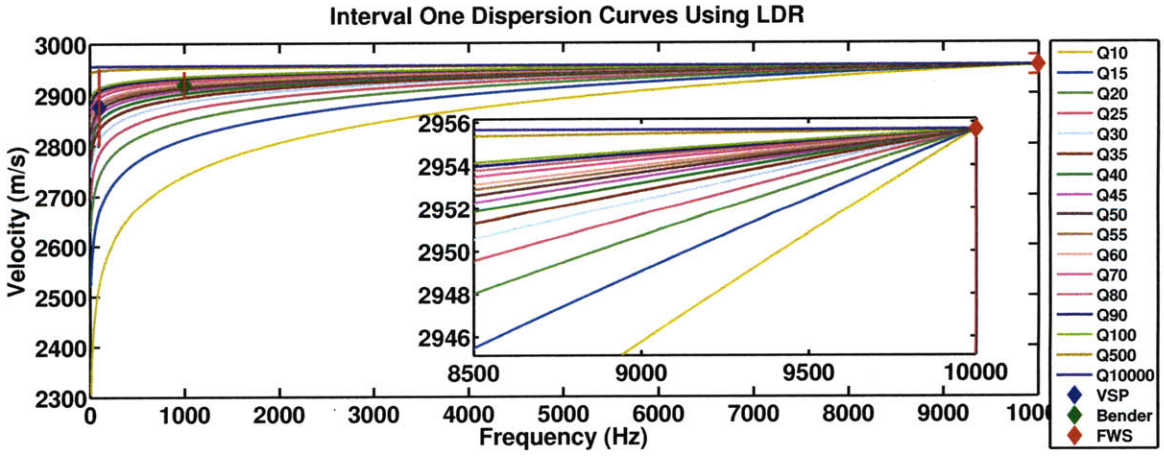

Figure 4.1: Dispersion curves for the first interval using LDR. The calculations are referenced to FWS with central frequency of 10000 Hz.

After calculating the dispersion curves, we use least squares to find the best Q that would

explain the field data. Table 4.1 shows that Q=54 is the best fit with the least error. Figure 4.2 was calculated using Q=54 and shows a good fit within the error bars. It is important to note that the VSP data quality sampling was coarse. In addition, we did not have access to the waveforms and assumed a central frequency of 100Hz; this is why the error is relatively large (around 76m/s). On a side note, we don't claim here that our Q estimation accuracy is in the range of ± 1. The reason we did these calculations is to provide a framework for finding the best Q.

	Slowness (μs/m)	**V_m(m/s)**	**V_r(m/s)**	ω	ω_r	**Q**	**V_c(m/s)**
VSP	347.77	2875.5	2959.2	100	10000	53	2873.9
Bender	341.21	2930.8	2959.2	1000	10000	53	2914.8
FWS	337.93	2959.2	2959.2	10000	10000	53	2955.6
VSP	347.77	2875.5	2959.2	100	10000	54	2878.9
Bender	341.21	2930.8	2959.2	1000	10000	54	2919
FWS	337.93	2959.2	2959.2	10000	10000	54	2959.2
VSP	347.77	2875.5	2959.2	100	10000	55	2880.3
Bender	341.21	2930.8	2959.2	1000	10000	55	2919.8
FWS	337.93	2959.2	2959.2	10000	10000	55	2959.2

Least Squares			
Q	**VSP**	**Bender**	**Total**
53	5.2964	12.3584	17.6548
54	**0.3272**	**9.8738**	**10.201**
55	4.4612	7.4796	11.9408

$\mathbf{V}_m$: Measured Velocity
$\mathbf{V}_r$: **Reference Velocity**
ω: Frequency
ω_r: Reference Frequency
$\mathbf{V}_c$: Calculated Velocity

Table 4.1: Velocity calculations and error using LDR for Q=53,54,55. The best fit with least error for VSP and Bender is Q=54

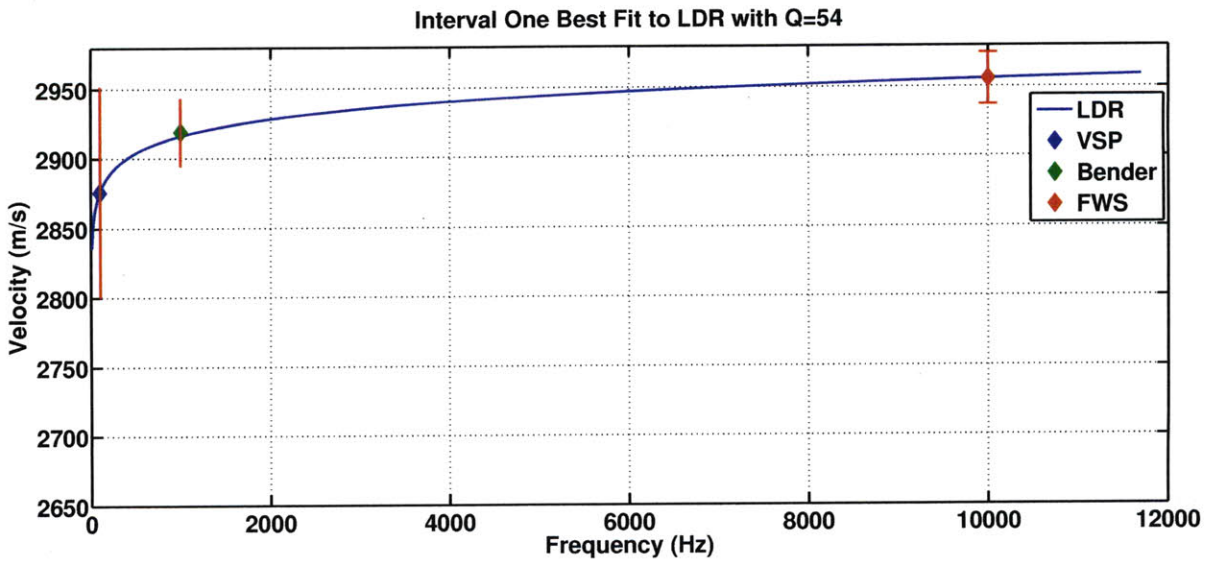

Figure 4.2: Field measurements fitted with Q=54

At this point, we have obtained a Q that explains the observed dispersion. However, we don't know the components of this Q as we basically fitted a curve through the field data, which presumably contains both components of the dispersion. Additionally, as mentioned earlier, the direct relation assumes plane waves propagating in a homogeneous model, which is not entirely true about this interval. This is where the DWN method becomes important. We will be able to separate the components of the dispersion through propagating twice; once in a heterogeneous medium and another in a homogeneous medium.

The dispersion curves for this interval obtained by DWN modeling are shown in figure 4.3. Changes in velocity as a function of Q from a reference frequency to a central frequency are presented in figure 4.4. The results are in agreement with LDR. In LDR, the reference velocity is the field measurement at the particular chosen reference frequency. On the other hand, in the DWN code, the reference velocity corresponds to the real part of the wave velocity at the particular reference frequency chosen (10kHz). Additionally, the imaginary part, which represents the attenuation in the wave propagation, is added to the real part. For the current frequency, the real part of the velocity is related to the velocity of the wave at the current frequency, while the imaginary part shows how much that wave will attenuate.

Consequently, there are some discrepancies between the two approaches. We believe that velocities obtained from modeling are more accurate as heterogeneity is considered.

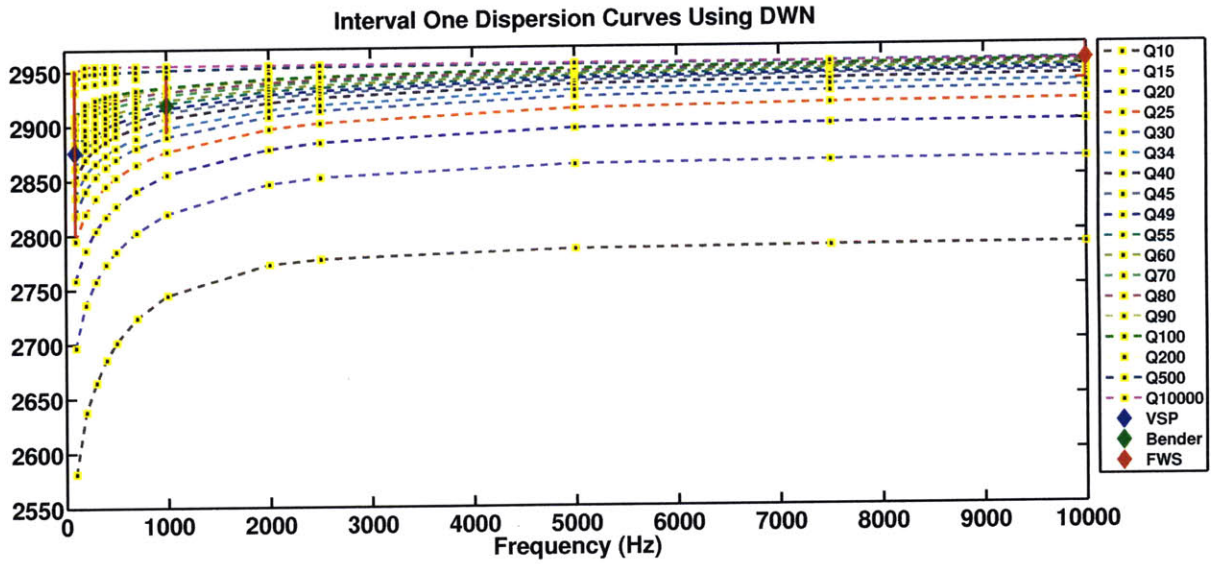

Figure 4.3: Interval one dispersion curves calculated using DWN

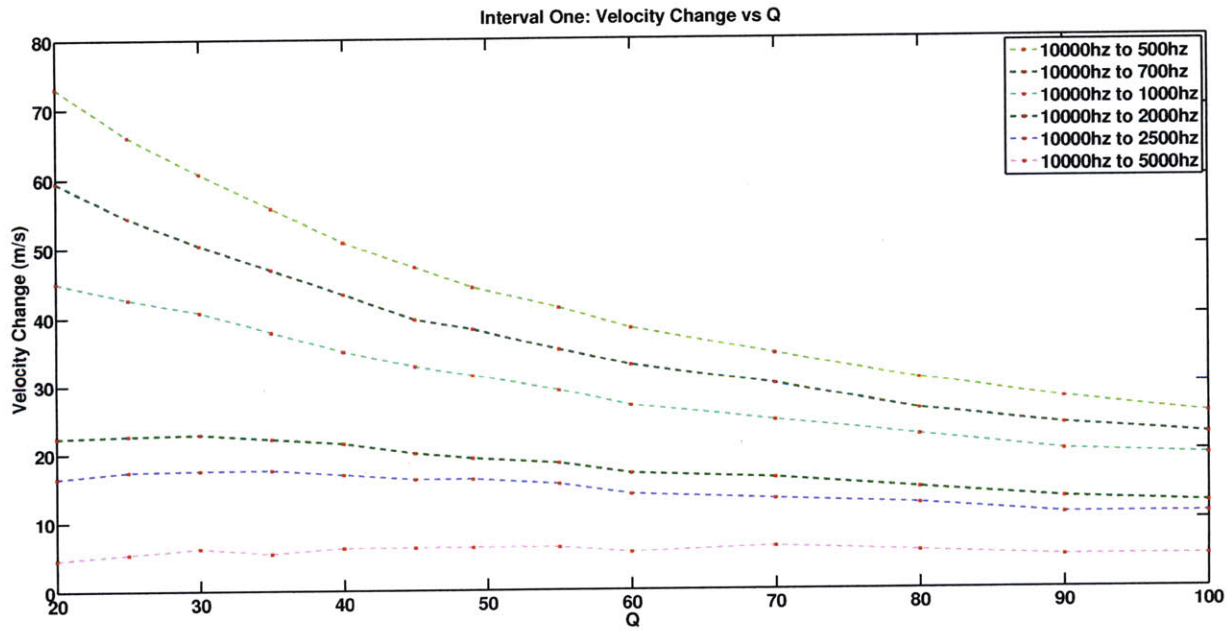

Figure 4.4: Changes in velocities from the reference frequency to central frequency as a function of Q

The overlaid seismograms in figure 4.5 are calculated with a central frequency of 1000 Hz and varying Q. As Q is increases, we see a shift and decreasing amplitude. Moreover, if

we look closely at the end of the seismogram we see very minimal scattering. This indicates that the Q=54 we obtained is mostly intrinsic attenuation. Figure 4.6 also confirms this result; it shows a very small difference between velocities from a homogeneous and a heterogeneous models. Finally, after ruling out elastic scattering as a component of the dispersion, we plotted the velocities from modeling along with directly calculated and field measured velocities in figure 4.7. The difference is well within the error bars.

Accounting for the possible measurement errors, Q ranges between 35 and 150 determined from the DWN and LDR dispersion curves. We determined this range from the Bender error bar. FWS error was not used because the calculations were referenced to it. The range is relatively large because the changes in velocity significantly decrease at Q>30 as can be seen in figure 4.1 and figure 4.4. Consequently, attenuation effects in this interval are minimal.

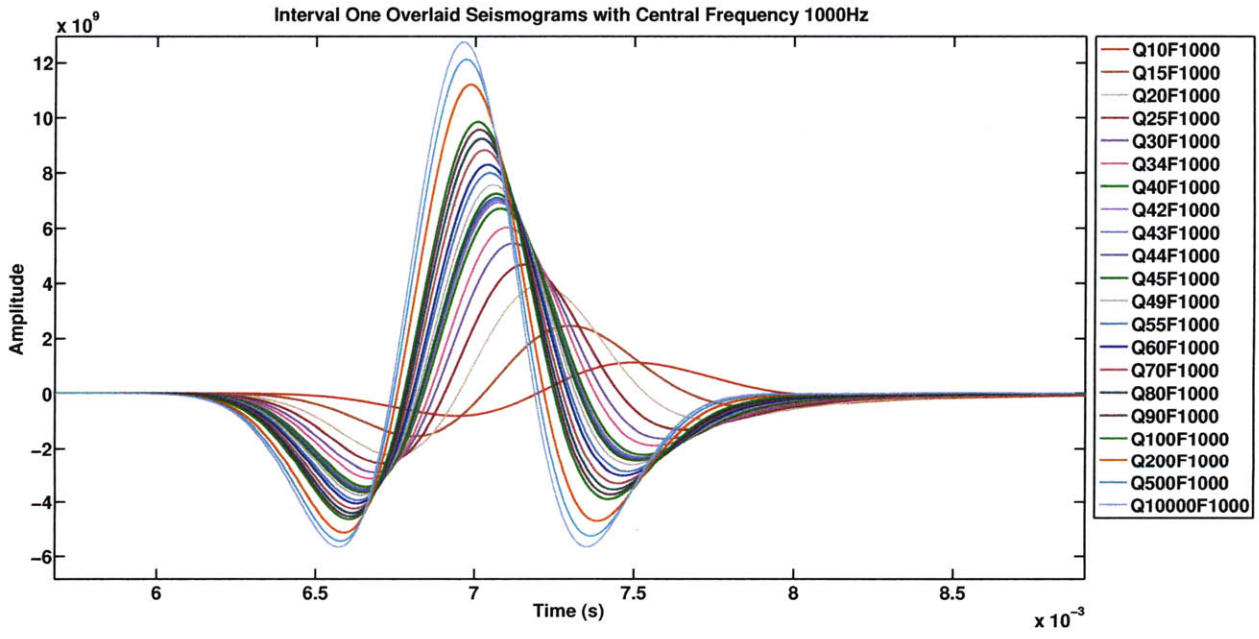

Figure 4.5: Overlaid seismograms with central frequency 1000Hz. Notice the shift as we increase Q

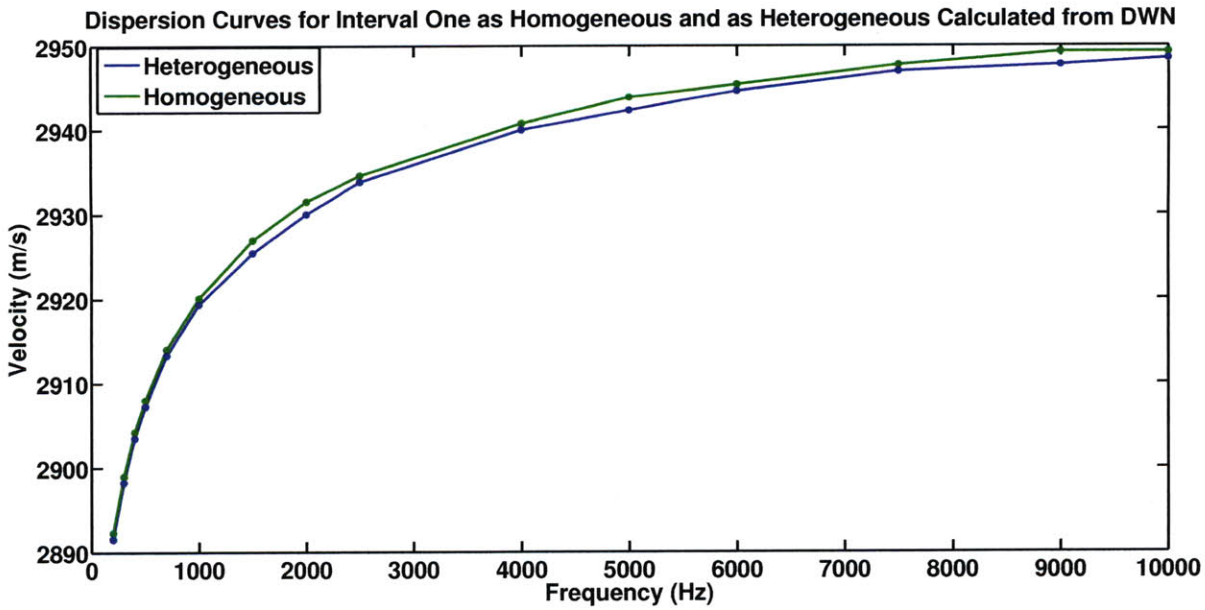

Figure 4.6: Dispersion curves for interval with a Q=54. The green curve represents velocities calculated from a homogeneous medium with average interval velocity obtained from average slowness. The blue curve represents velocities calculated from a heterogeneous model (both curves are calculated using the DWN). The difference is very small which confirms our conclusion that the observed dispersion is mainly caused by intrinsic attenuation.

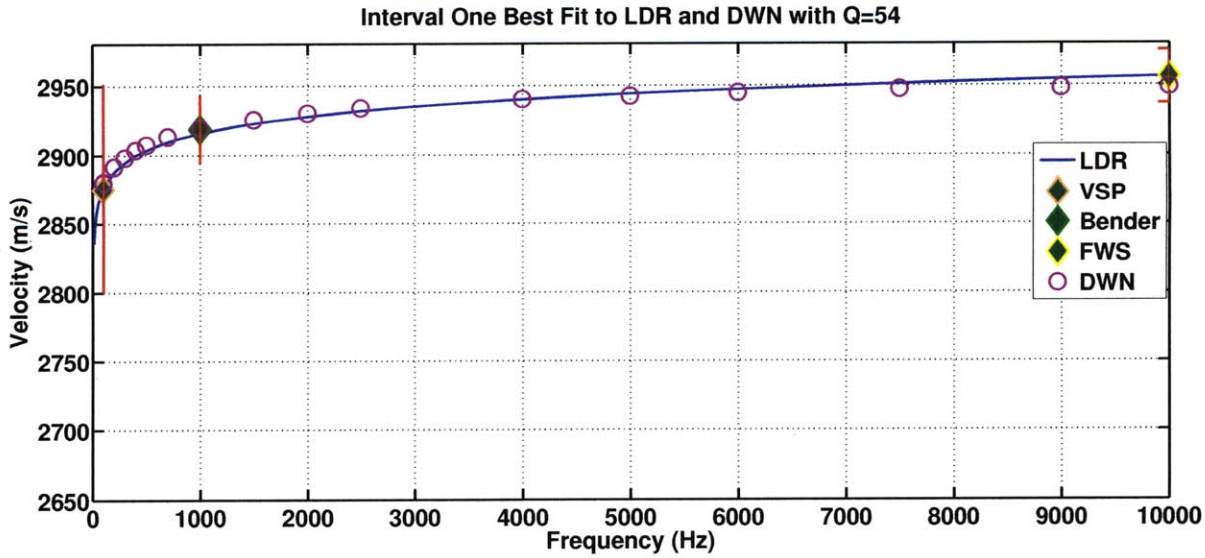

Figure 4.7: Final result for interval one. Intrinsic Q=54 best explains the dispersion

4.2 Interval Two

This interval is the "Gypsy Sandstone" interval and is predominantly sandstone/siltstone. Figure 4.8 shows the results from the LDR. Table 4.2 shows that Q=35 is the best fit with the least error considering VSP and Bender jointly. Figure 4.9 was calculated using Q=35 and shows a good fit within the error bars. The dispersion curves for this interval obtained by DWN modeling are shown in figure 4.10. The difference is a bit larger for this interval than the previous interval. One possible reason for this is that the Gypsy interval is composed of stacked channels. The overlaid seismograms in figure 4.12 are calculated with a central frequency of 1000 Hz and varying Q. We plotted the velocities from modeling along with directly calculated and field measured velocities in figure 4.13. Brown and Seifert (1997) estimated $Q_{intrinsic}$=31 which is close to what we estimated. Finally, accounting for the measurement errors, Q ranges between 25 and 55. The range is shorter in this interval because it is more heterogeneous than the first interval.

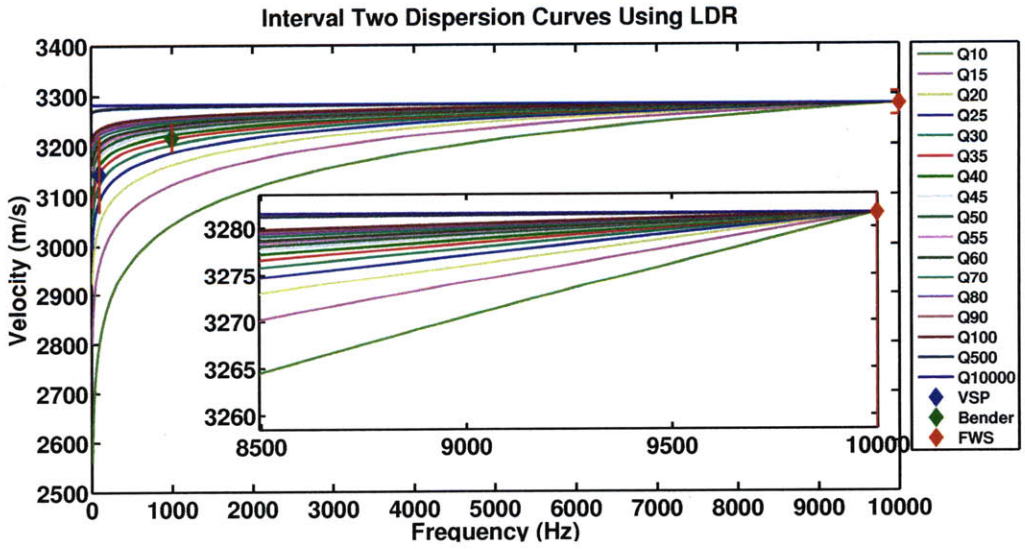

Figure 4.8: Dispersion curves for the second interval using LDR. The calculations are referenced to a frequency of 10000Hz which is roughly the FWS central frequency.

	Slowness (μs/m)	V_m(m/s)	V_r(m/s)	ω	ω_r	Q	V_c(m/s)
VSP	3142.3	3142.3	3277.4	100	10000	34	3136
Bender	3208.4	3208.4	3277.4	1000	10000	34	3206.7
FWS	3277.4	3277.4	3277.4	10000	10000	34	3277.4
VSP	3142.3	3142.3	3277.4	100	10000	35	3140.1
Bender	3208.4	3208.4	3277.4	1000	10000	35	3208.8
FWS	3277.4	3277.4	3277.4	10000	10000	35	3277.4
VSP	3142.3	3142.3	3277.4	100	10000	36	3143.9
Bender	3208.4	3208.4	3277.4	1000	10000	36	3210.7
FWS	3277.4	3277.4	3277.4	10000	10000	36	3277.4
Least Squares Interval Two							
Q	**VSP**	**Bender**	**Total**				
34	7.7204	13.0672	20.7877				
35	**5.5481**	**6.433**	**11.9811**				
36	18.0794	0.1673	18.2467				

Table 4.2: velocity calculations and error using LDR for Q=34,35,36. The best fit with least error for VSP and Bender is Q=35.

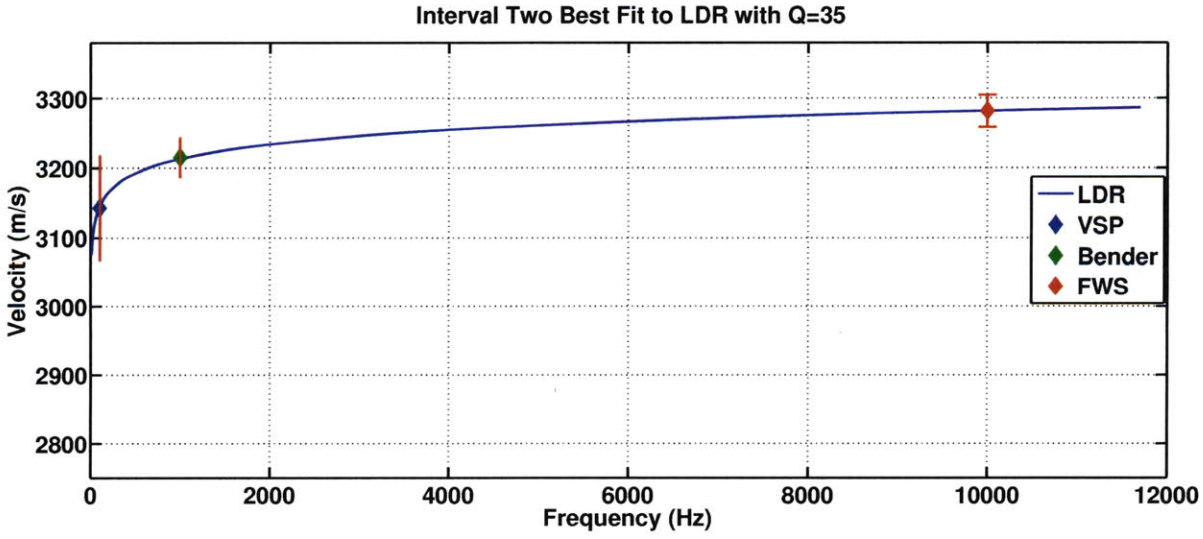

Figure 4.9: Field measurements fitted with LDR with Q=35

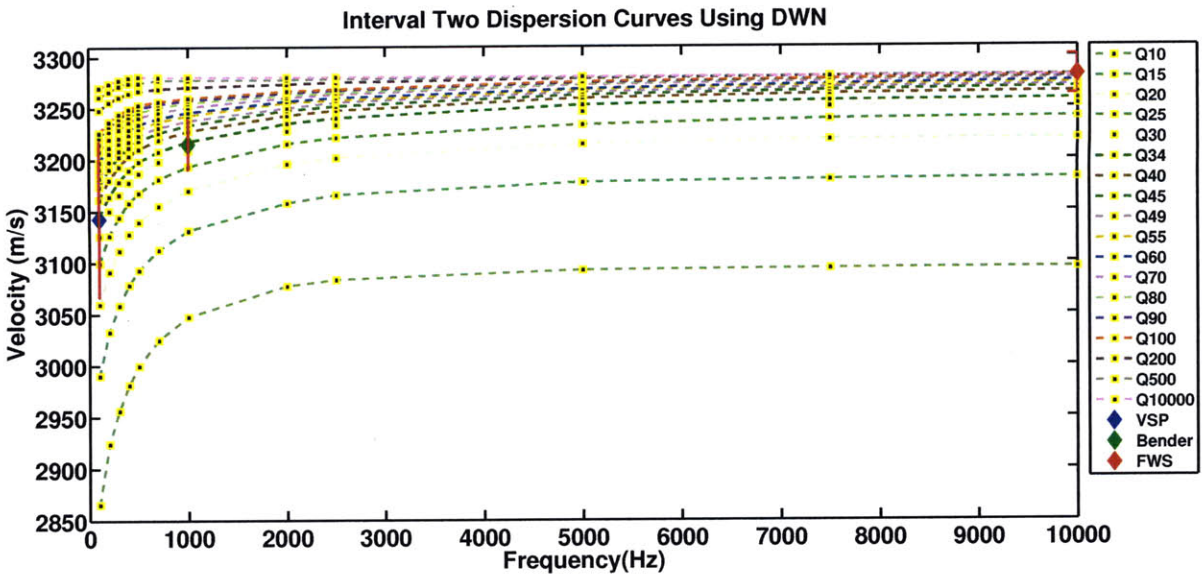

Figure 4.10: Interval Two dispersion curves calculated using DWN

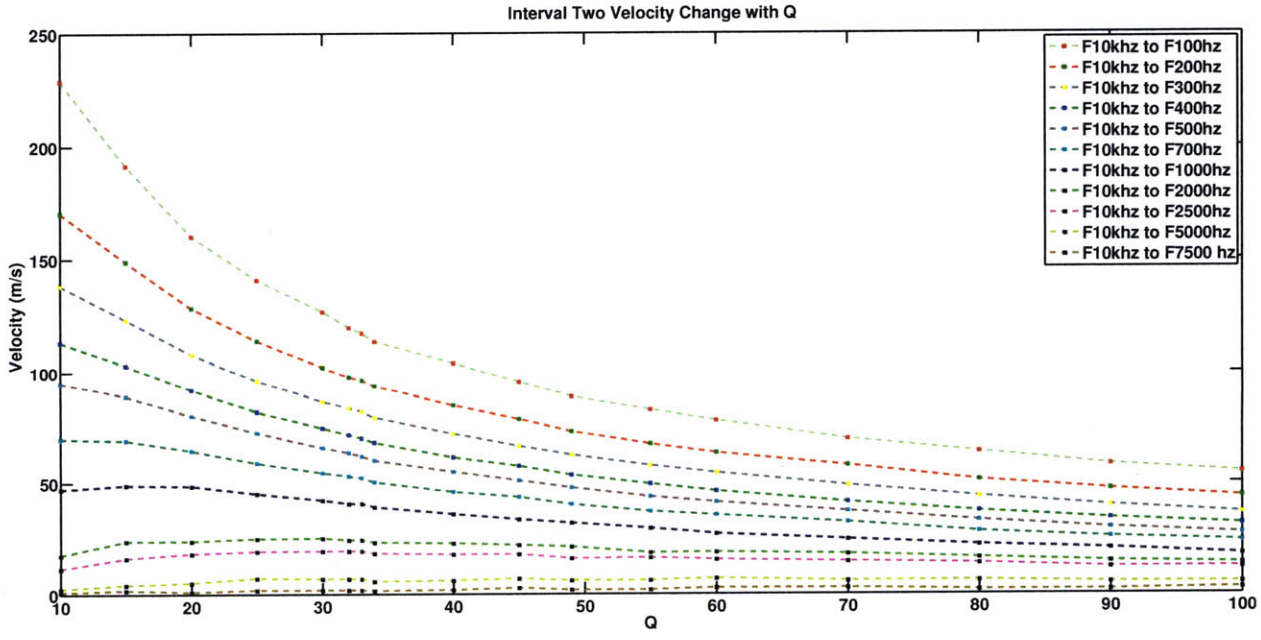

Figure 4.11: Changes in velocities from the reference frequency to central frequency as a function of Q

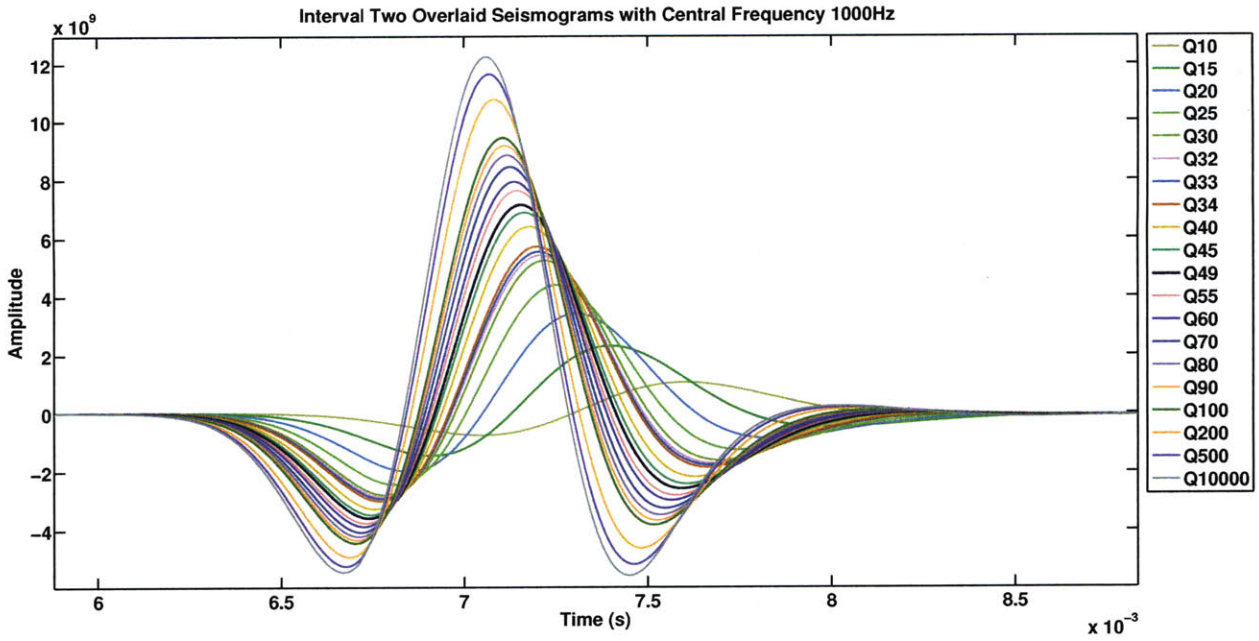

Figure 4.12: Overlaid seismograms with central frequency 1000Hz. Notice the shift as we increase Q

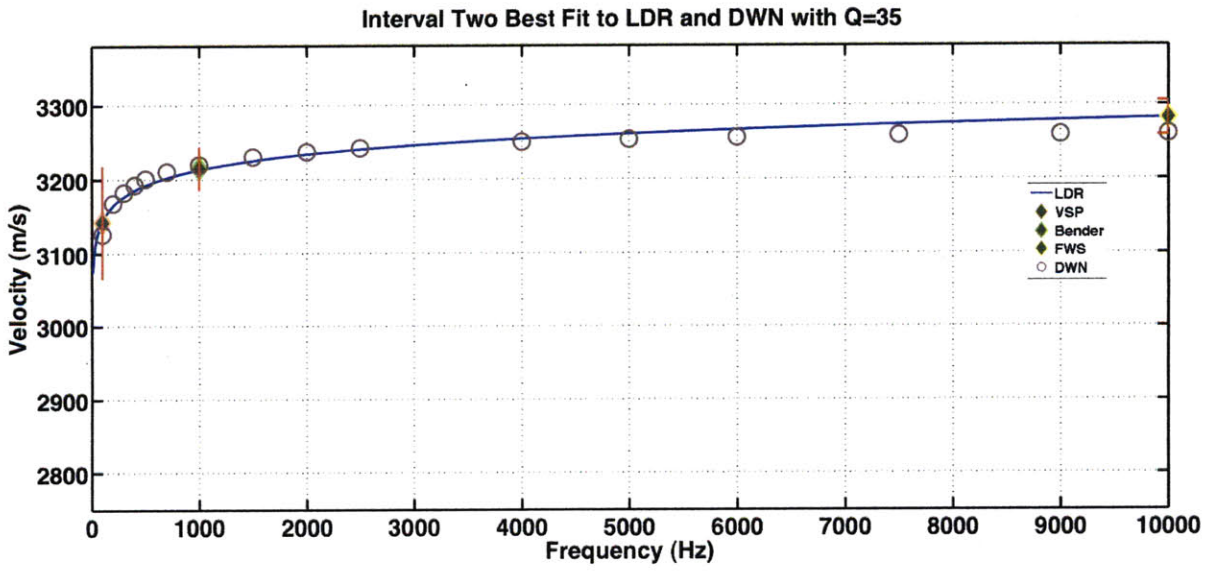

Figure 4.13: Dispersion curves for interval with a Q=35. The green curve represents velocities calculated from a homogeneous medium with average interval velocity obtained from average slowness. The blue curve represents velocities calculated from a heterogeneous model (both curves are calculated using the DWN). The difference is very small which confirms our conclusion that the observed dispersion is mainly caused by intrinsic attenuation.

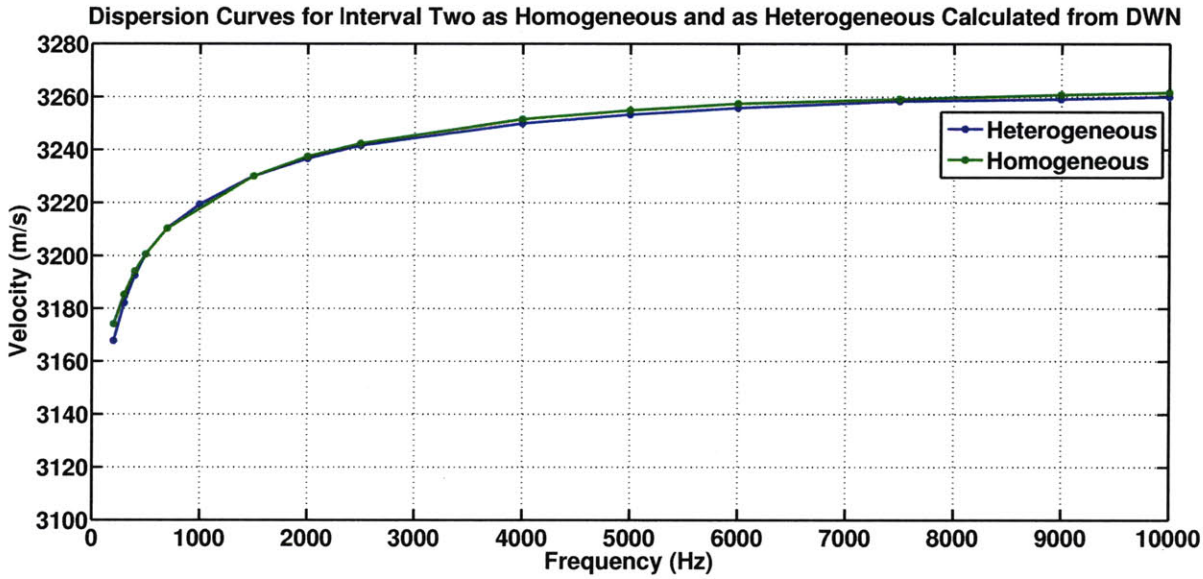

Figure 4.14: Final result for interval two. Intrinsic Q=35 best explains the dispersion

4.3 Interval Three

This interval is the comes after the Gypsy sandstone interval. It is mainly composed of shale and sandstone. Figure 4.15 shows the results from the LDR. Table 4.3 shows that Q=28 is the best fit with the least error considering VSP and Bender jointly. Figure 4.16 was calculated using Q=28 and shows a good fit within the error bars. The dispersion curves for this interval obtained by DWN modeling are shown in figure 4.17. Changes in velocity as a function of Q from a reference frequency to a central frequency are presented in figure 4.18. The overlaid seismograms in figure 4.19 are for a central frequency of 1000Hz and varying Q. Figure 4.21 shows a very small difference between velocities from a homogeneous and a heterogeneous models. Figure 4.20 show the velocities from modeling along with directly calculated and field measured velocities. Finally, accounting for the measurement errors, Q

ranges between 20 and 35. The even shorter range in this interval relative to the first and second intervals is due to higher attenuation.

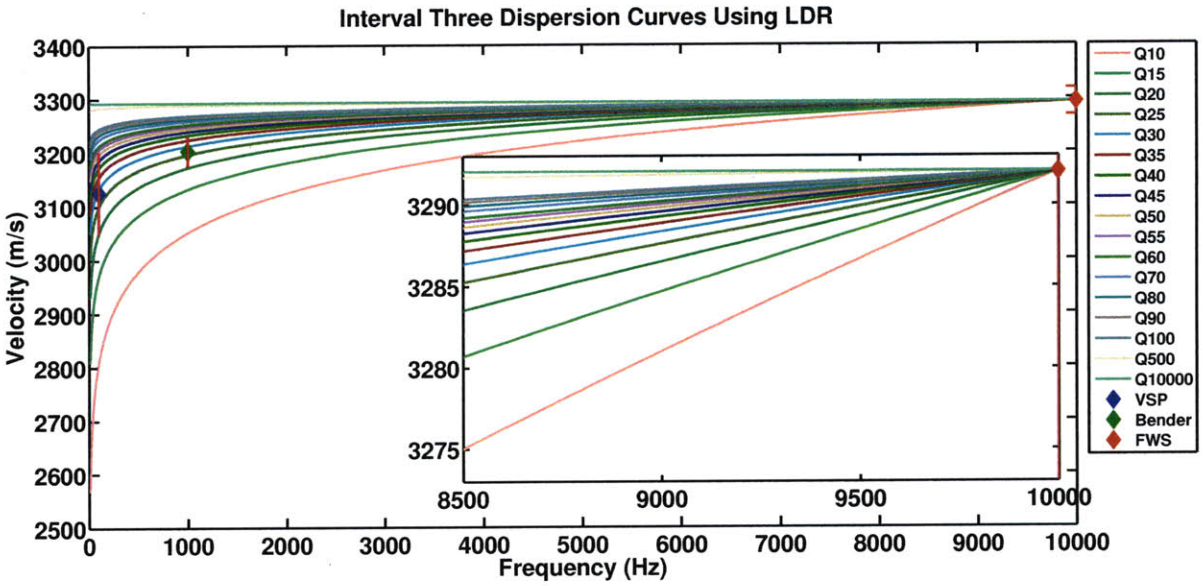

Figure 4.15: Dispersion curves for the second interval using LDR. The calculations are referenced to a frequency of 10000Hz which is roughly the FWS central frequency

	Slowness (μs/m)	V_m(m/s)	V_r(m/s)	ω	ω_r	Q	V_c(m/s)
VSP	3110.2	3110.2	3349.5	100	10000	27	3167.5
Bender	3208.4	3208.4	3349.5	1000	10000	27	3258.5
FWS	3349.5	3349.5	3349.5	10000	10000	27	3349.5
VSP	3110.2	3110.2	3349.5	100	10000	28	3174
Bender	3208.4	3208.4	3349.5	1000	10000	28	3261.7
FWS	3349.5	3349.5	3349.5	10000	10000	28	3349.5
VSP	3110.2	3110.2	3349.5	100	10000	29	3180.1
Bender	3208.4	3208.4	3349.5	1000	10000	29	3264.8
FWS	3349.5	3349.5	3349.5	10000	10000	29	3349.5

Least Squares Interval Three			
Q	**VSP**	**Bender**	**Total**
27	36.9049	1.4721	38.377
28	**0.0699**	**0.0563**	**0.1262**
29	3.5559	21.7025	25.2584

Table 4.3: Velocity calculations and error using LDR for Q=27,28,29. The best fit with least error for VSP and Bender is Q=28.

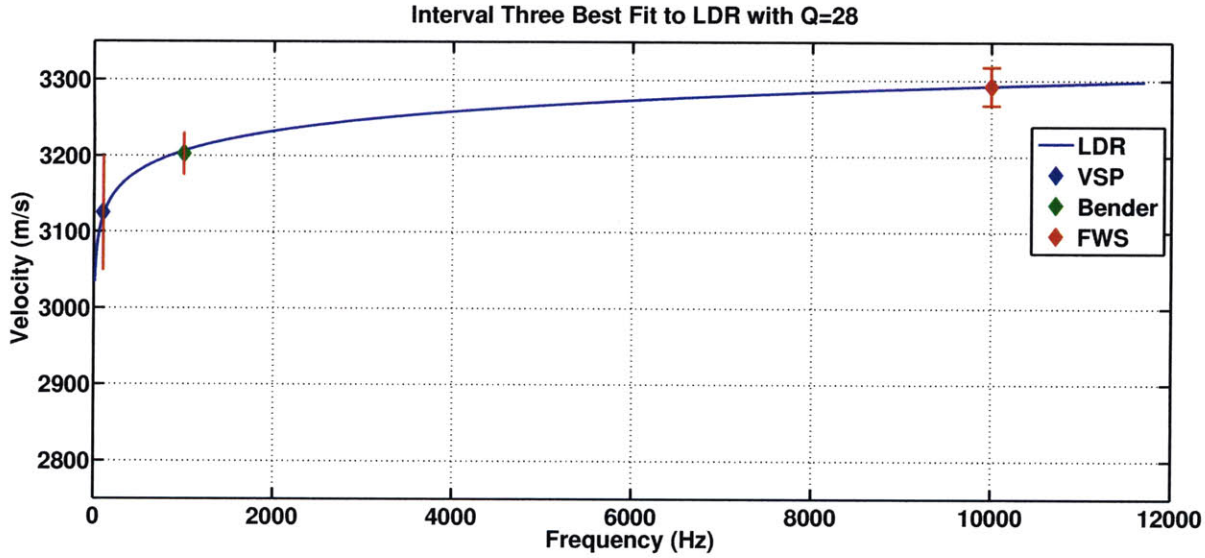

Figure 4.16: Field measurements fitted with Q=28

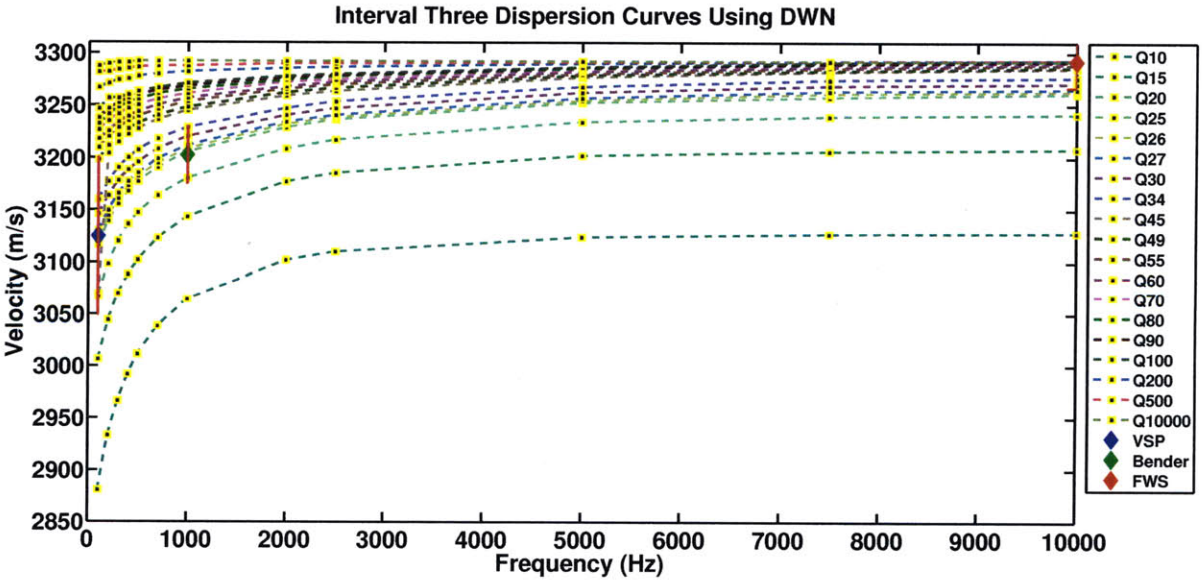

Figure 4.17: Interval Three dispersion curves calculated using DWN

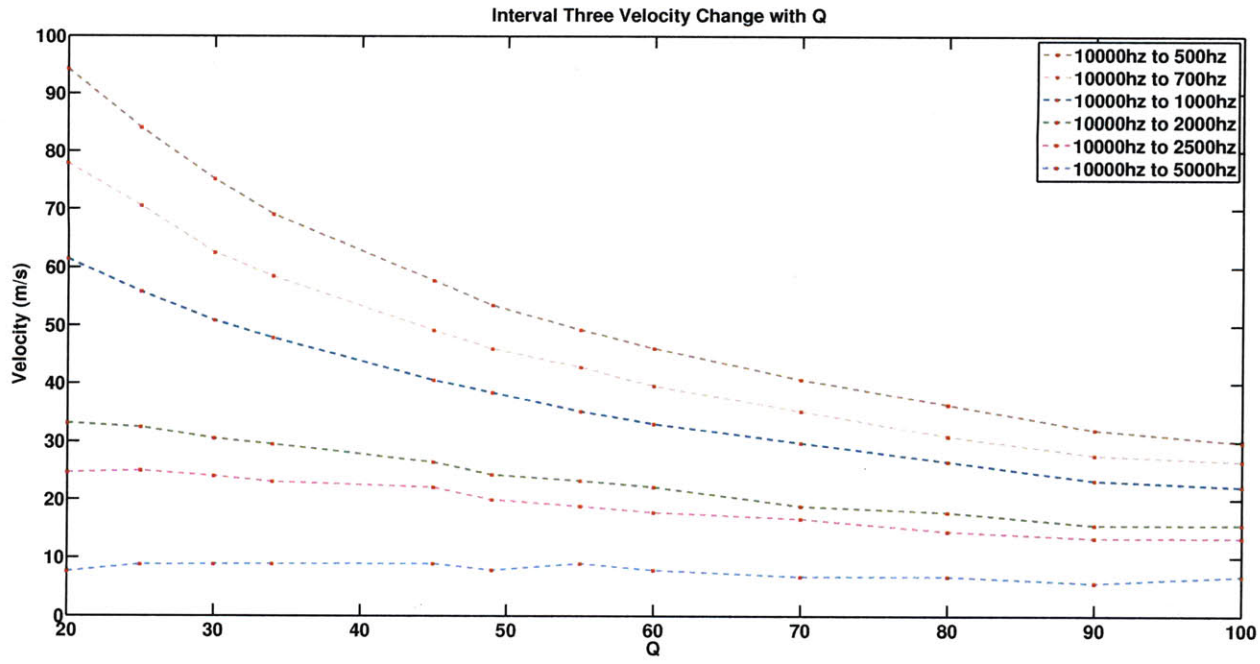

Figure 4.18: Changes in velocities from the reference frequency to central frequency as a function of Q

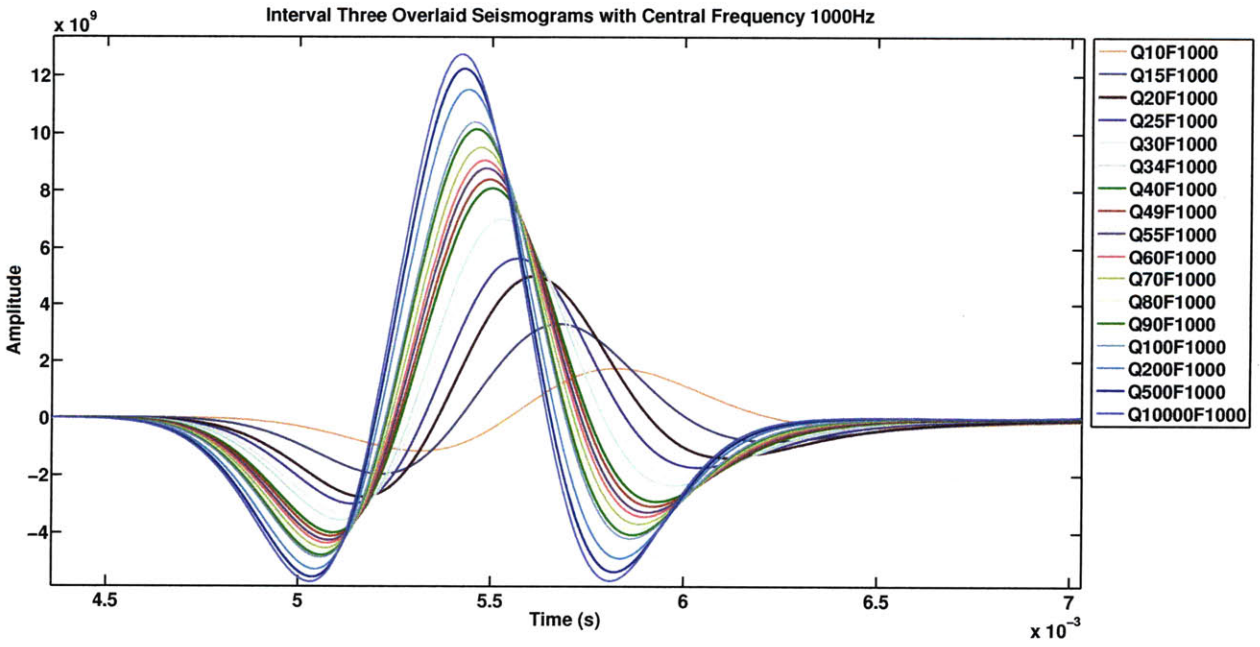

Figure 4.19: Overlaid seismograms with central frequency 1000Hz. Notice the shift as we increase Q

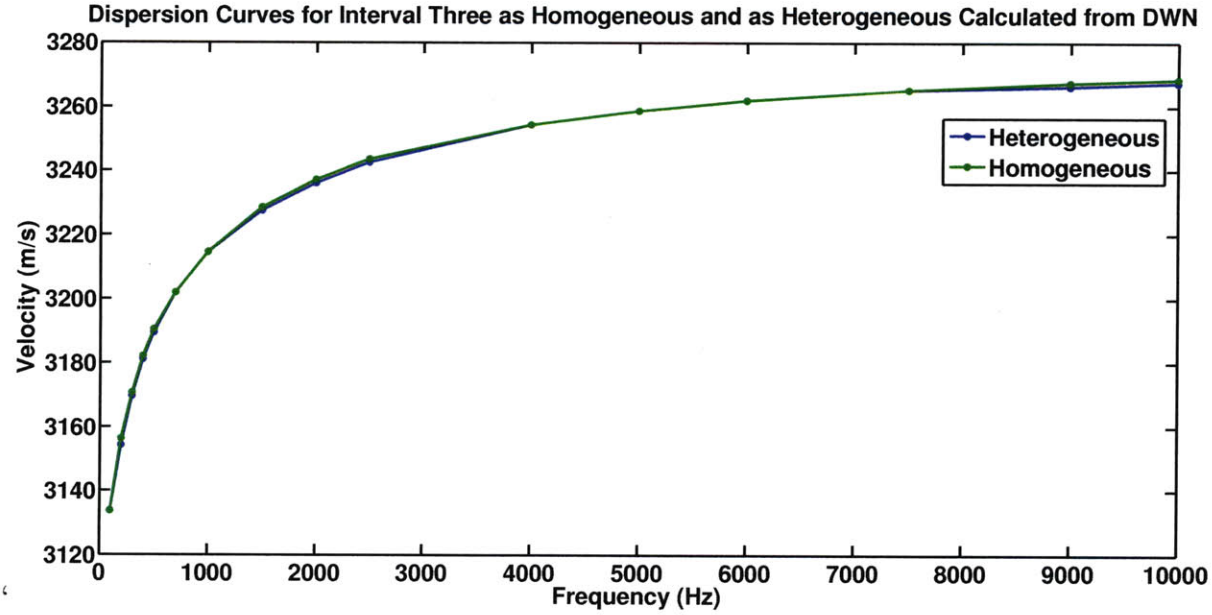

Figure 4.20: Dispersion curves for interval with a Q=28. The green curve represents velocities calculated from a homogeneous medium with average interval velocity obtained from average slowness. The blue curve represents velocities calculated from a heterogeneous model (both curves are calculated using the DWN). The difference is very small which confirms our conclusion that the observed dispersion is mainly caused by intrinsic attenuation.

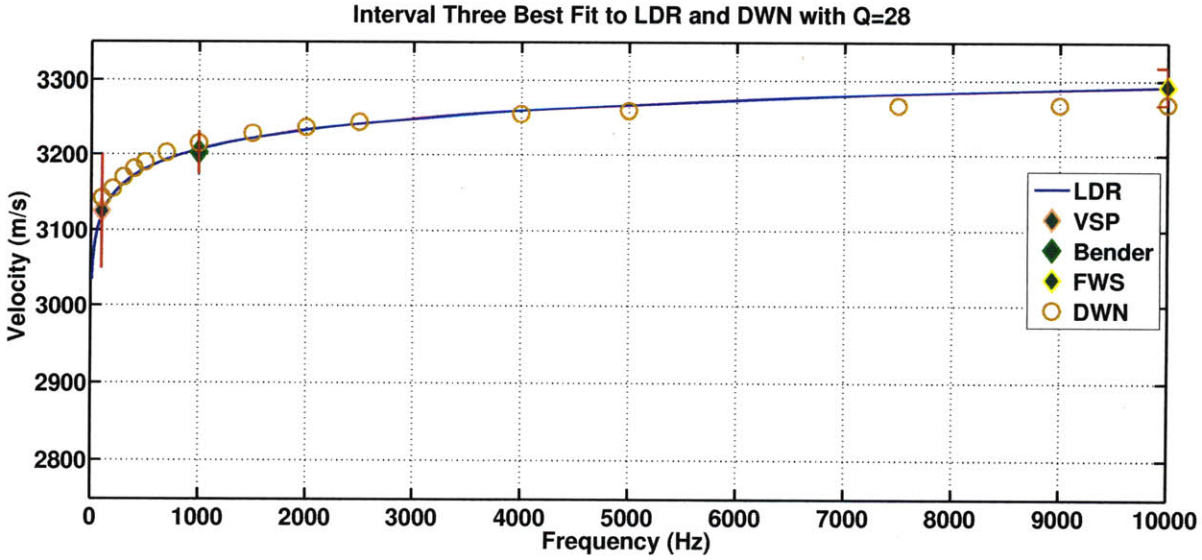

Figure 4.21: Final result for interval three. Intrinsic Q=28 best explains the dispersion

4.4 Interval Four

This interval includes Gypsy sandstone interval and the marine fluvial interval below it. It is mainly composed of shale and sandstone. Figure 4.22 shows the results from LDR. Table 4.4 shows that Q=30 is the best fit with the least error considering VSP and Bender jointly. Figure 4.23 was calculated using Q=28 and shows a good fit within the error bars. The dispersion curves for this interval obtained by DWN modeling are shown in figure 4.24. Changes in velocity as a function of Q from a reference frequency to a central frequency are presented in figure 4.25. The overlaid seismograms in figure 4.26 are for a central frequency of 1000 and varying Q. Figure 4.28 shows a very small difference between velocities from a homogeneous and a heterogeneous models (0.5%). Figure 4.22 shows the final result. Finally, the Q error range is between 25 and 50.

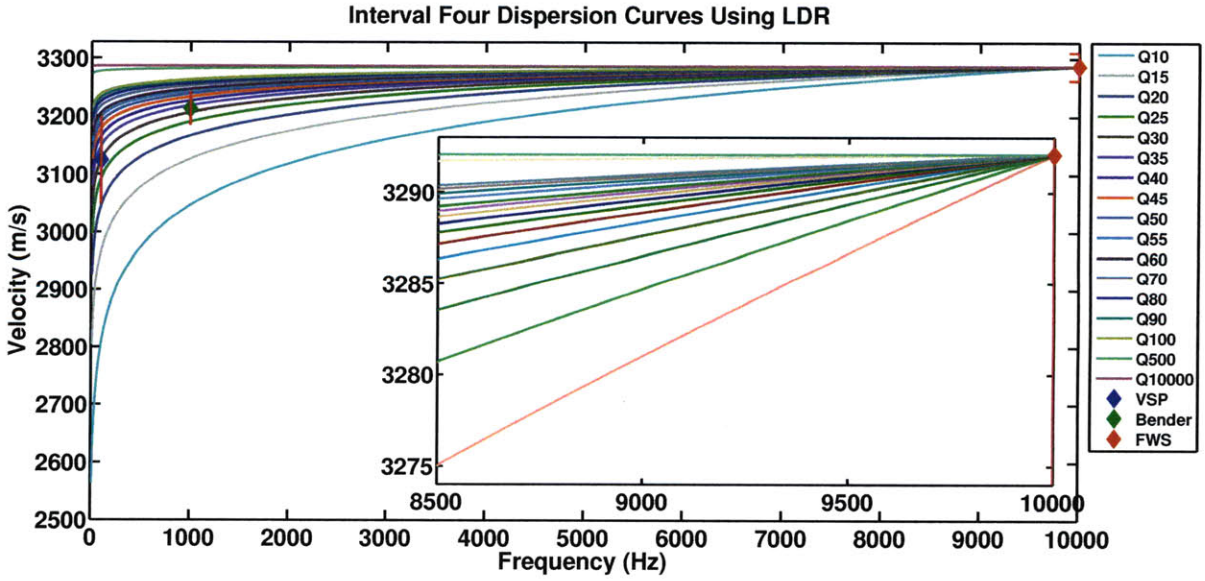

Figure 4.22: Dispersion curves for the first interval using LDR. The calculations are referenced to a frequency of 10000Hz which is roughly the FWS central frequency

	Slowness(m)	V_m(m/s)	V_r(m/s)	ω	ω_r	Q	V_c(m/s)
VSP	2875.5	3124.1	3286.1	100	10000	29	3119.9
Bender	2930.8	3212.8	3286.1	1000	10000	29	3203
FWS	2959.2	3286.1	3286.1	10000	10000	29	3286.1
VSP	2875.5	3124.1	3286.1	100	10000	30	3125.4
Bender	2930.8	3212.8	3286.1	1000	10000	30	3205.7
FWS	2959.2	3286.1	3286.1	10000	10000	30	3286.1
VSP	2875.5	3124.1	3286.1	100	10000	31	3130.6
Bender	2930.8	3212.8	3286.1	1000	10000	31	3208.3
FWS	2959.2	3286.1	3286.1	10000	10000	31	3286.1

Least Squares Interval Four			
Q	**VSP**	**Bender**	**Total**
29	13.8189	32.2491	46.0680
30	**4.3553**	**23.1620**	**27.5173**
31	21.3570	14.6611	36.0181

Table 4.4: Velocity calculations and error using LDR for Q=29,30,31. The best fit with least error for VSP and Bender is Q=30.

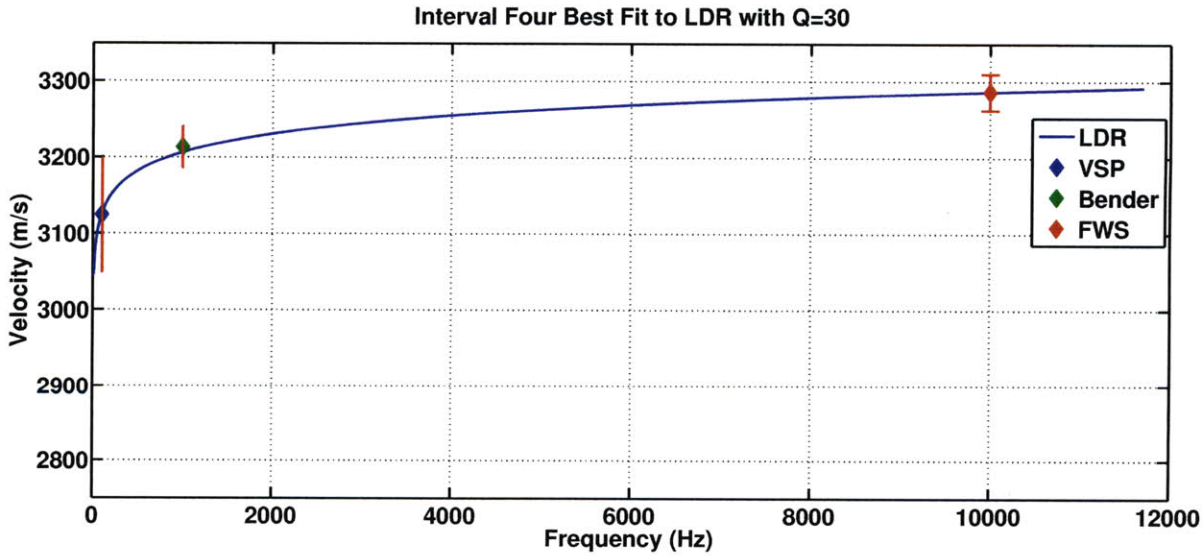

Figure 4.23: Field measurements fitted with LDR, Q=30

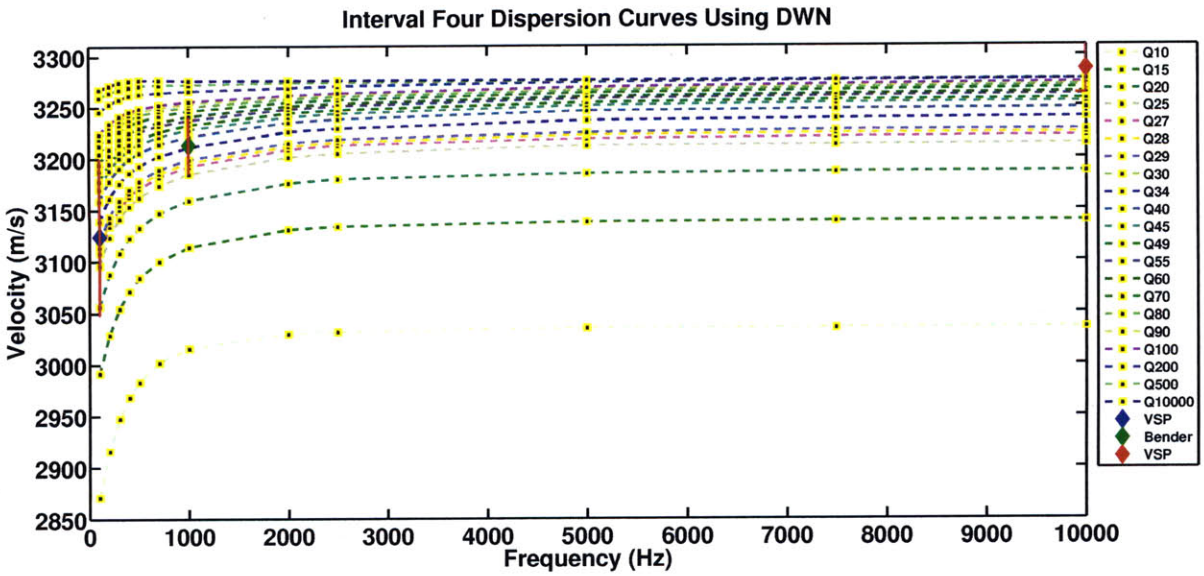

Figure 4.24: Interval four dispersion curves calculated using DWN

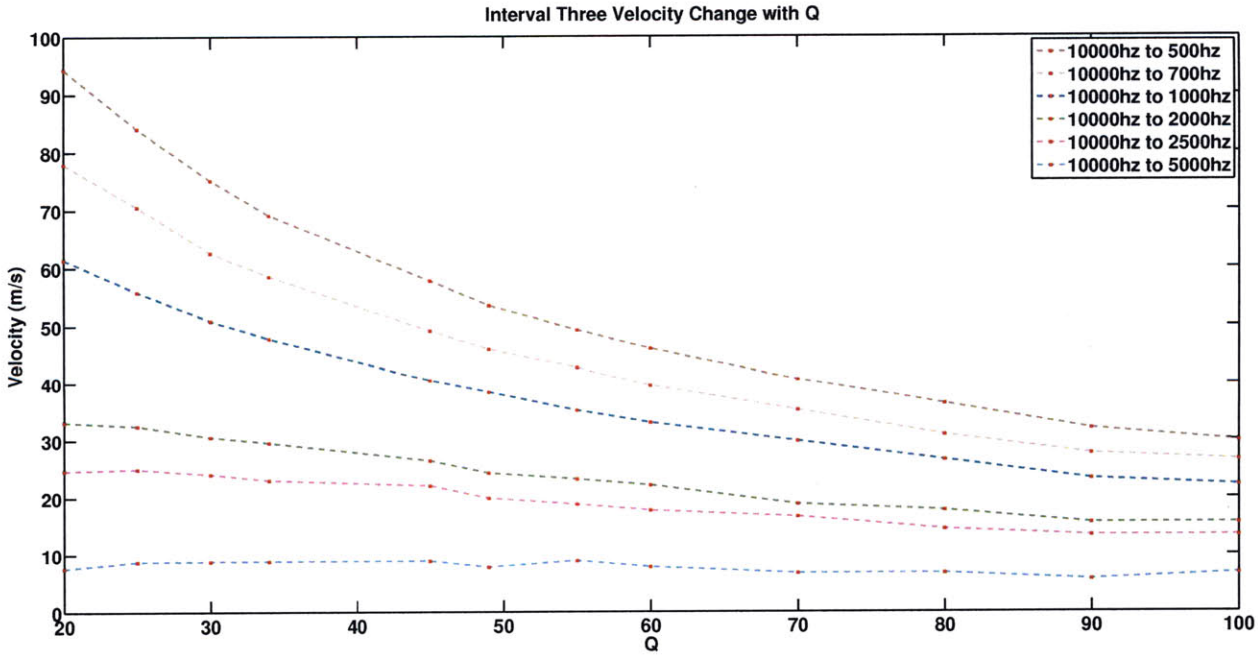

Figure 4.25: Changes in velocities from the reference frequency to central frequency as a function of Q

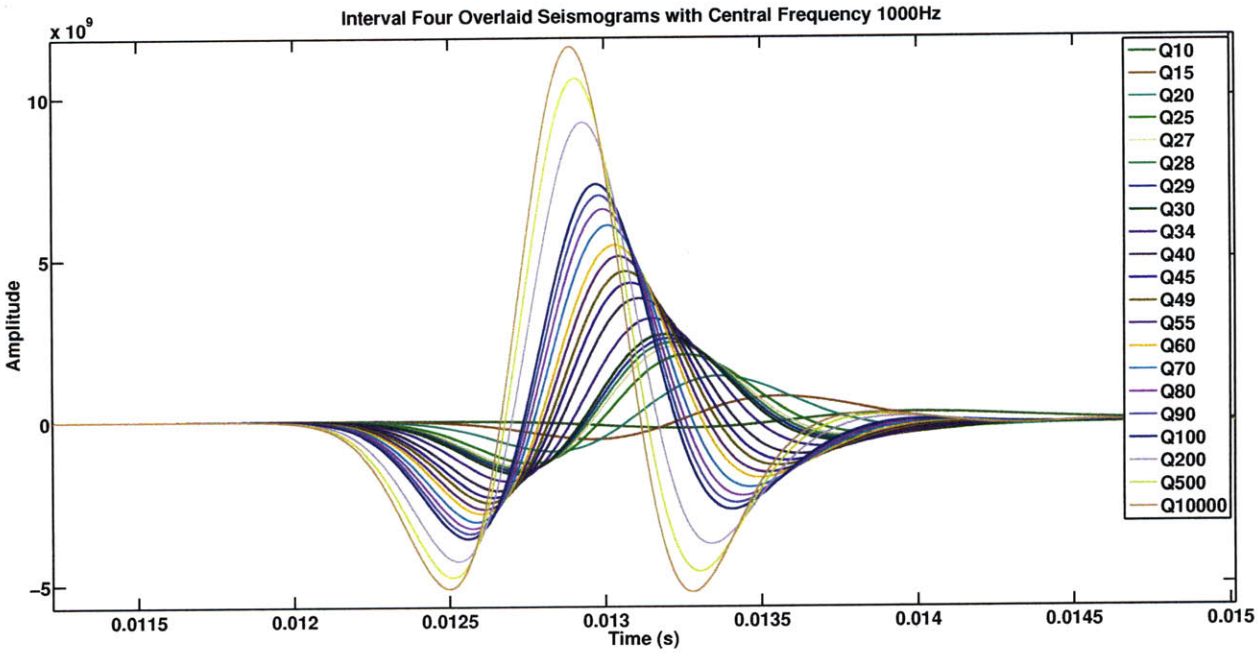

Figure 4.26: Overlaid seismograms with central frequency 1000Hz

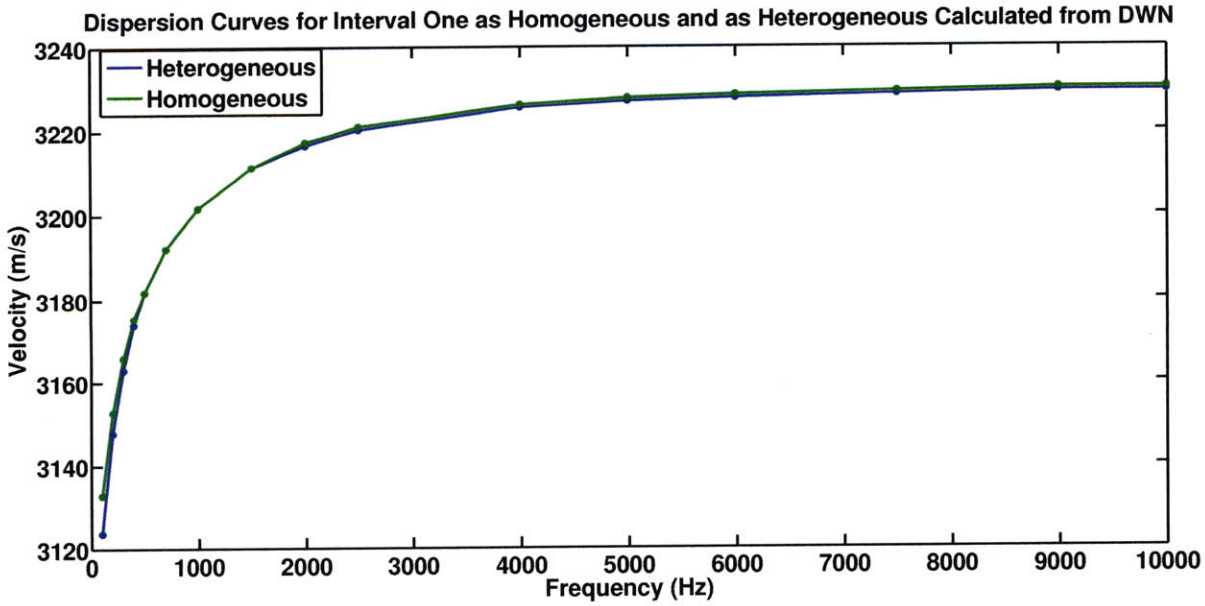

Figure 4.27: Dispersion curves for interval four with a Q=30. The scattering component in this interval is 0.5%

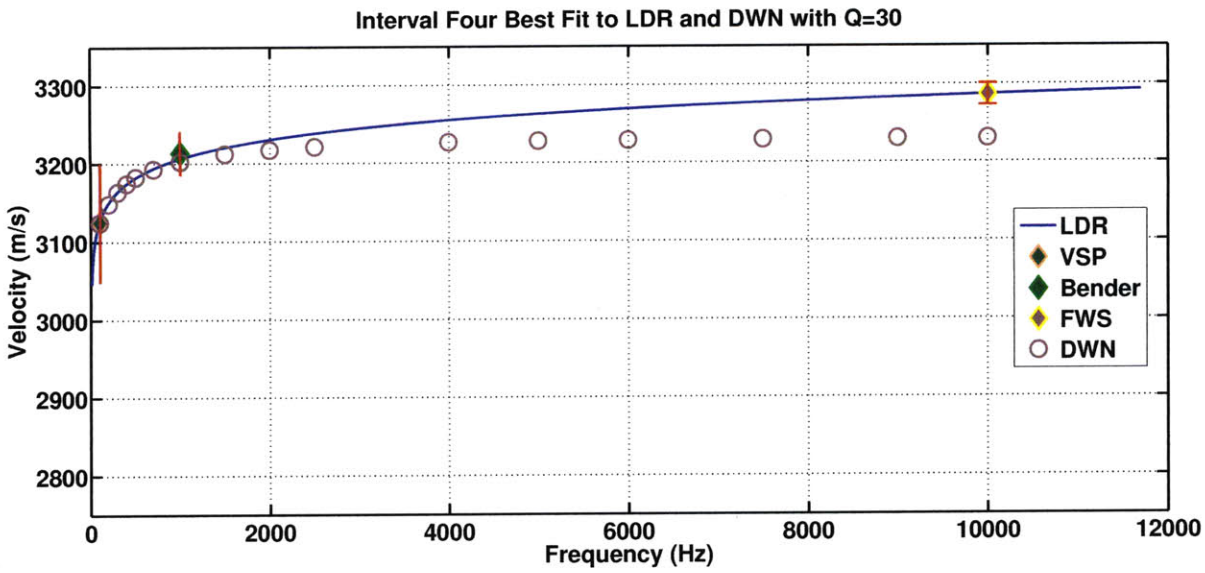

Figure 4.28: Final result for interval four. Intrinsic Q=30 best explains the dispersion.

4.5 Summary of Results and Discussion

Using LDR and DWN, we were able to find an effective Q for each interval that best describes the observed dispersion. We estimated Q_I=54, Q_I=35, Q_I=28, and Q_I=30, for the first, second, third and fourth intervals, respectively. We accounted for measurements' errors by providing a range of Q values that are within the error bars of the Bender log. We did not use FWS error as in both approaches it is assigned as the reference source (velocity and frequency). Since the VSP error is the largest, all Q values within the Bender's error range go through the VSP error. The Q error ranges is dependent on how attenuative the medium is; the more attenuative the medium is, the shorter the Q error range is. This is due to velocity changes decreasing as Q increases.

Through modeling each interval twice; once as heterogeneous and another as homogeneous, we showed that the scattering effects for vertical propagation in Gypsy site are minimal could be neglected, and that the main cause of the observed dispersion is intrinsic attenuation. Our conclusion is in agreement with that of Brown and Seifert (1997) and De et al. (1994).

The differences in estimating velocities using the DWN method and LDR are primarily due to the way the reference velocity is treated. In LDR, the reference velocity is fixed, while in DWN it is variable for each layer. Since the DWN method account for heterogeneity, we believe that it is more accurate and provides more information (i.e. scattering effects, waveforms) at relatively cheap cost compared to other methods of wave propagation such as finite differences and finite elements. However, it is important to note that the DWN only works with layered media.

Aside from intrinsic attenuation and elastic scattering, other factors contributing to the dispersion include volume differences, path effects, and measurement errors (Brown and Seifert, 1997). The measurement errors could be reduced by careful repicking and processing of the first arrivals. Moreover, estimating the central frequency is extremely important and will yield to better results. Since we did not have access to the waveforms, we assumed the central frequencies to be what the field source frequency is. For example, we estimated the FWS central frequency by counting events from a hard copy of the waveforms (figure 3.7) and obtained values between 7500Hz to 16000Hz. This wide range introduces an additional error in estimating Q.

Chapter 5

Conclusion

We were presented with a data set from Gypsy Site that showed discrepancies in velocity measurements from different sources for the same interval. We chose three intervals with different properties and depositional environments. The first interval was predominantly shale and the second interval was mostly sandstone, while the third interval was a mix of both. Additionally, we modeled the second and third intervals combined which showed the effects of elastic scattering that we did not observe when modeling the three intervals with an average thickness of 20m. We started our investigation of this problem with logarithmic dispersion relation. Using this direct relation, we were able to estimate a constant Q value that best explains the observed dispersion in different intervals. However, on one hand, this equation assumes that plane waves propagate in an infinitely homogeneous medium, and on the other hand, the constant Q value is chosen based on least squares curve fitting of the measured field data. Thus, the estimated Q value will include both scattering and intrinsic attenuation effects. Consequently, we needed another approach that involves wave propagation that could explain the observed dispersion while accounting for the heterogeneity of the medium. Using the DWN, we were able to use the Q we obtained from the direct relation in estimating the dispersion components. This was accomplished by modeling the interval twice, one as a heterogeneous medium and another as a homogeneous medium (average interval velocity).

The difference between the calculated arrival times (if any) indicates that elastic scattering is part of the causes of the observed discrepancies.

Our results indicate that for the three intervals with an average thickness of 20m each, the elastic scattering component of the dispersion is minimal. We believe that intrinsic attenuation is largely the main cause of the observed dispersion. This conclusion is largely consistent with the work done on the same field by Brown and Seifert (1997). We believe that the Gypsy sandstone interval could be explained by intrinsic Q=35, compared with a Q=31 by Brown and Seifert. This difference is mainly due to slightly different thicknesses (our interval was shorter). Additionally, both Q values are within the velocity measurement error range. Moreover, De et al. (1994), showed that elastic scattering could be neglected in vertical propagation when the medium is shale/sand, which is also consistent with our results.

The methods and steps we used in the identification and modeling of velocity dispersion provide key information in reservoir characterization. Estimation and separation of the dispersion components can be used as an indicator to rock properties.

5.1 Future Work

Velocity dispersion is a problem because it presents a challenge in using data from different source frequencies to estimate the seismic response at higher or lower frequencies. The identification and modeling of velocity dispersion becomes especially important in integrating different types of data such as subsurface cores and VSP and using it in reservoir characterization. As we have shown in this thesis, velocity dispersion is indicative of intrinsic attenuation and elastic scattering especially for vertical measurements; and since these two mechanisms are related to rock properties such as porosity, permeability, hydrocarbons, fluids...etc, it is an excellent tool in exploration seismology. While the data we had and methods we used were sufficient to show and model the observed velocity dispersion, there is still much

room for improvement; for future work we recommend the following:

1. Seek access to more acquired data such as digital surface seismic, VSP, Bender and FWS waveforms to correctly estimate the central frequency band.

2. Seek access to the acquired crosswell data to measure the dispersion from horizontal propagation using finite difference method. This will help in understanding more about the anisotropic component of the dispersion.

3. Reprocess the data and repick arrival times from the waveforms.

4. Use different Q values for different types of rocks. This could be achieved by using information from the Gamma log, cores, slownesses...etc to identify the main types of rocks.

5. Apply and compare other dispersion models such as: Cole-Cole, Muller, Kolsky-Futterman, and Kjartansson.

Bibliography

Aki, K., Richards, P. G., 1980, Quantitative seismology, Vol. 1: W. H. Freeman and Co.

Batzle, M. L.,D.H.Han, and R. Hofmann, 2006, Fluid mobility and frequency- dependent seismic velocity—Direct measurements: Geophysics, 71, no 1, N1–N9.

Bouchon M. 2003. A review of the Discrete Wavenumber Method [J]. Pure Appl Geophys, 160(03): 445–465.

Bouchon, M. (1979), Discrete Wavenumber Representation of Elastic Wave Fields in Three-space Dimensions, J. Geophys. Res. 84, 3609–3614.

Bouchon, M. and Aki, K. (1977), Discrete Wave-number Representation of Seismic Source Wave Fields, Bull. Seismol. Soc. Am. 67, 259–277.

Brajanovski, M., T. Müller, and B. Gurevich, 2006, Characteristic frequencies of seismic attenuation due to wave-induced fluid flow in fractured porousmedia: Geophysics Journal International, 166, 574–578.

Brown, R. L., and Seifert, D., 1995, Velocity dispersion: a problem and a solution: 65th Ann. Internat. Mtg. Soc. Expl. Geophys., Expanded Abstracts, 663–666.

Brown, R. L., and Seifert, D., 1997, Velocity dispersion: a tool for characterizing reservoir rocks. Geophysics 62, pp. 477–486.

Burns D. R., and Martin R. J. III, 1993, Elastic Property Scaling Relationships and the Seismic Characterization of Reservoir Flow Units - A Feasibility Approach, New England Research, Inc.

De, S. G., Winterstein, D. F., and Meadows, M. A., 1994, Comparison of P-wave and S-wave velocities and Q's from VSP and sonic log data: Geophysics, 59, 1512–1529.

Doyle, J.D. and Sweet, ML., "Three–Dimensional Distribution of Lithofacies, Bounding Surfaces, Porosity, and Permeability in a Fluvial Sandstnne-Gypsy Sandstone of Northern Oklahoma", AAPG. Bull. (Jan. 1995) 79. No. 1.70.

Doyle, J. D., O'Meara, D. J., and Witterholt, E. J., 1992, The "Gypsy" field research program in integrated reservoir characterization, SPE 24710, 67th Ann. Technical Conference and Exhibition: Soc. Petr. Eng.

Futterman,W. I., 1962, Dispersive body waves: Journal of Geophysical Research, 67, 5279–5291.

Parra J.O., B.J. Zook, H.A. Collier, "Interwell Seismic Logging for Formation Continuity at the Gypsy Test Site, Oklahoma," Journal of Applied Geophysics, Vol. 35, No. 1, pp. 45-62, 1996.

Johnson, D. L., 2001, Theory of frequency dependent acoustics in patchysaturated porous media: Journal of theAcoustical Society of America, 110, 682–694.

Klimentos, T, 1995, Attenuation of P- and S-waves as a method of distinguishing gas and condensate from oil and water: Geophysics,60. 447-458

Knopoff, L., and G. J. F. MacDonald, 1958, Attenuation of small amplitude stress waves in solids: Review of Modern Physics, 30, 1178–1192.

Marion, D., Mukerji, T., and Mavko, G., 1994, Scale effects on velocity dispersion: From ray to effective medium theories in stratified media, Geophysics, 59, 16 13-l 6 19.

Mavko, G., T. Mukerji, and J. Dvorkin, 1998, The rock physics handbook: Cambridge University Press.

Melia, P. J., and Carlson, R. L., 1984, An experimental test of P-wave anisotropy in stratified media: Geophysics, 49, 374-378.

Mukerji, T., Mavko, G., Mujica, D., and Lucet, N., 1995, Scale dependent seismic velocity

in heterogeneous media: Geophysics, 60, 1222–1233.

Liao, Q. and G. A. McMechan, Tomographic imaging of velocity and Q, with application to crosswell seismic data from the Gypsy Pilot Site, Oklahoma, Geophysics, 62, 1804-1811, 1997.

Pride, S. R., and J. G. Berryman, 2003, Linear dynamics of double-porosity dual-permeability materials: 1—Governing equations and acoustic attenuation: Physical Review, E68, 036603.

Schoenberger, M., and Levin, F. K., 1974. Apparent attenuation due to intrabed multiples, Geophysics, 39, 278-291.

Sidorovskaia, N. A., Lockard, E. S., "Velocity Dispersion as a Tool for Reservoir Imaging," Proceedings of the Sixth Latin American and Caribbean petroleum Engineering Conference, Caracas, Venezuela, 21-23 April, 1999.

Spencer, J. W., 198 1, Stress rexations at low frequencies in fluid-saturated rocks: Attenuation and modulus dispersion: J. Geophys. Res., 86, 1803-l 8 12.

Stein and M. Wysession, An Introduction to Seismology, Earthquakes and Earth Structure, 2003, Blackwell Publishing, Oxford, 498 pp., ISBN 0-86542- 078-5

Stewart, R.R., P.D. Huddlestone and T.K. Kan, Seismic versus sonic velocities: a vertical seismic profiling study. Geophysics 49 (1984), pp. 1153–1168.

Sun, L.F., Milkereit, B., and Schmitt, D.R., 2009, Measuring velocity dispersion and attenuation in the exploration seismic frequency band: Geophysics, 74, WA113-WA122.

Turpening, W. R., Y-T. Chon, R. E. F. Pepper, R. Szerbiak, T. Schultz, G. Thielmier, and R. Ballard, 1992, Detection of bed continuity using crosswell data: a Gypsy pilot site study: Society of Petroleum Engineers 67th Annual Technical Conference and Exhibition, Washington, D.C., October 4-7, p. 503-511.

Varela, C. L., Rosa, A. L., and Ulrych, T. J., 1993, Modeling of attenuation and dispersion: Geophysics, 58, 1167–1173.

White, J. E., 1975, Computed seismic speeds and attenuation in rocks with partial gas saturation: Geophysics, 40, 224–232.

Winkler, K. E., and Nur, A., and 1979, Friction and seismic attenuation rocks: Nature, 277,528.53 1.

Yamamato, T., Nye, T., and M., 1994, Porosity, permeability, shear strength: Crosswell tomography below an iron foundary: Geophysics, 59 1530-1541.

Zener, C. M., 1948, Elasticity and anelasticity of metals: University of Chicago Press.

Appendix A

DWN Code

In this appendix, we will show how to run the DWN code by Michel Bouchon, input parameters, and the output file.

A.1 DWN Input File

The input file consists of the following 23 parameters:

1. Number of layers including the half-space
2. Layers thicknesses (km)
3. P-wave velocity (km/s)
4. S-wave velocity (km/s)
5. Layer density
6. Quality factor for the P-wave
7. Quality factor for the S-wave
8. Hypocenter depth (source location)

(a) Expressed in km

(b) Must be greater than the receivers depth

9. Strike of the fault a. Measured clockwise from the North b. Expressed in km

10. Dip of the fault (km)

11. Rake

(a) Measured counter clockwise from the strike

(b) Defined as the slip direction of the foot wall relative to the hanging wall

12. Amplitude of the Slip

(a) Can be expressed with the desired unit for the output displacement or velocity

13. Length of the fault (km)

14. Number of receivers

15. Depth of receivers

(a) Expressed in km

(b) All receivers will be located at the same depth

16. Distance of each receiver (horizontal distance from the source)

17. Azimuth of each receiver

18. Number of points of the seismogram(s)

(a) Must be expressed in 2^n

(b) It should be > 8*recording time*frequency. Under sampling will cause Gibbs phenomenon (figure 1)

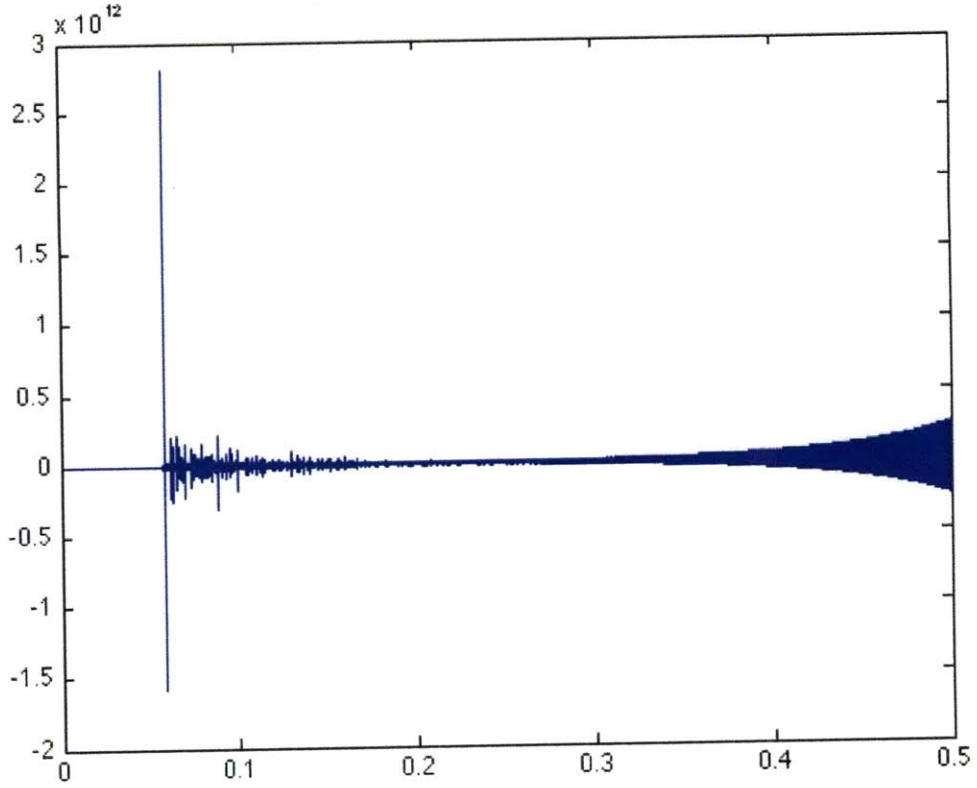

Figure A.1: The growing noise toward the end of the recording window is known as Gibbs phenomenon. In the particular case of this graph, it was caused by under sampling. Choosing a low rise time of the slip to yield higher frequencies and not accounting for it in determining the sampling rate, will lead to this problem as well.

19. Recording time (s)

20. Rise time of the slip

    (a) We use it to control the source central frequency

    (b) If the output is velocity, then the central frequency is 2/frequency

    (c) If the output is Displacement, then the central frequency is 1/frequency

21. Starting time of recording

22. Maximum truncation index of the wavenumber series.

(a) Is the maximum wavenumber

(b) Must be greater than the wavenumber to avoid the possibility of truncation occurrence (>1.5*frequency/Minimum velocity).

23. Periodicity length

(a) Must be >Maximum Velocity*recording time + Maximum Receiver distance. Otherwise the seismogram will fold.

Apart from the input file, we have changed the reference frequency to 10000Hz from 1Hz. This is because we have a field measurement at that frequency and half of the source frequencies we are using are in the kHz range. Additionally, the code originally uses the moment tensor derived from strike, slip, dip and rake of the fault; we have changed it to an explosion source by manually designating the moment tensor as follows:

CM11=1;

CM22=1;

CM33=1;

CM12=0;

CM13=0;

CM23=0;

The following is a typical input file we used to model our data with the definition of each parameter to the right:

Input file	Parameters definition
119	Number of layers
1 2.944074181 1.766444509 2.54 26 13	Layer thickness, P-wave velocity, S-wave velocity,
0.00016764 2.944074181 1.766444509 2.54 26 13	P-wave Quality factor and S-wave Quality factor,
0.0001524 2.911174785 1.746704871 2.55 26 13	
0.0001524 2.911174785 1.746704871 2.56 26 13	
0.0001524 2.816745218 1.690047131 2.56 26 13	
0.0001524 2.87900255 1.72740153 2.57 26 13	
0.00012192 2.960948125 1.776568875 2.56 26 13	
0.00018288 2.944074181 1.766444509 2.54 26 13	
0.0001524 3.029821074 1.817892644 2.53 26 13	
0.0001524 2.944074181 1.766444509 2.54 26 13	
0.0001524 2.944074181 1.766444509 2.56 26 13	
0.0001524 2.944074181 1.766444509 2.57 26 13	
.	
.	
.	
.	
0.00012192 3.236699586 1.942019752 2.56 26 13	
0.00018288 3.196979232 1.918187539 2.56 26 13	
0.0001524 3.029821074 1.817892644 2.56 26 13	
0.0001524 3.047390522 1.828434313 2.56 26 13	
0.00012192 3.047390522 1.828434313 2.56 26 13	
0.00018288 3.047390522 1.828434313 2.57 26 13	
0.0001524 3.029821074 1.817892644 2.57 26 13	
1 3.029821074 1.817892644 2.57 26 13	
1.01784604	Source depth
0 90 180	Strike, Dip, Rake
1	Amplitude of Slip
1	Length of fault
1 1	Number of receivers, depth of receivers
0.0000001 1	Distance of receivers, Azimuth of receivers
8192 0.015	Number of points, Window length
0.001 0	Rise time of slip, start time
1048576 5000	Maximum truncation index, Periodicity length

Table A.1: DWN Input file

It is for the third interval of interest. The reason we padded the model with a 1000m thick layer is to eliminate free surface and rigid surface effects to simulate a zero-offset field survey. The source is placed at the to of the bottom 1000m layer at a depth of 1017.8m and

the receiver is placed at the bottom of the top 1000m layer at a depth of 1000m. Our models are 1D and wave propagation is 1-way from an explosion source, thus, assigning any value for the strike, dip, rake, slip and the azimuth of the receiver will yield to the same results; we used 0,90,180,1 and 1 respectively. The length of the fault will affect the amplitude of the seismogram, we used a consistent value (1) for all models. We used 0.01m as the horizontal distance of the receiver from the source because 0 will produce null results. The rise time of the slip is 0.001 to simulate a central frequency of 1000Hz. Finally, we used a large for the periodicity length to insure the seismogram won't fold in itself.

A.2 Compiling and Running the DWN code

The DWN code was written in Fortran and the computations are performed serially. The user must have a recent version of a Fortran compiler; we used the GNU Fortran compiler. Running and compiling the code could be expressed by the following two lines syntax:

gfortran –O3 –o JobName Filename.f

./JobName

Example:

gfortran –O3 –o Int1HomogCase DWNexplosion.f

./Int1HomogCase

-O3 option is for optimization. While a personal machine could handle the computations, we opted to use MIT Zephyr cluster to oversample the seismograms and avoid problems like Gibbs Phenomenon. The average running time on a 2.0Ghz CPU for a model consisting of 150 layers is 2 hours with a sampling rate of 8192 and a recording time of 0.015seconds.

A.3 DWN Output File

Below is an output file from the input file used an example above. The output file consists of three vectors:

1. Index of the receiver (1=x-component, 2=y-component, 3=z-component).
2. Time
3. Amplitude

1 0.000000 0.000000
1 1.8310546E-06 3.8661528E-07
1 3.6621093E-06 7.7718869E-07
.
.
.
.
1 1.4995827E-02 0.3022113
1 1.4997658E-02 0.3024174
2 0.000000 0.000000
2 1.8310546E-06 6.8066583E-09
2 3.6621093E-06 1.3588760E-08
2 5.4931638E-06 2.0379957E-08
.
.
.
.
2 1.4995827E-02 5.2751531E-03
2 1.4997658E-02 5.2787587E-03
3 0.000000 0.000000
3 1.8310546E-06 -36.53125
3 3.6621093E-06 -93.50000
.
.
.
.
3 1.4993996E-02 -4.7244832E+07
3 1.4995827E-02 -4.7272432E+07
3 1.4997658E-02 -4.7302032E+07

Table A.2: Output File

A.4 Plotting Seismograms and Picking First Arrivals

We used Matlab to plot the seismograms and pick the first arrival. Because our wavelet is a zero-phase Ricker wavelet with its peak at t=0, we picked the maximum amplitude as the

first arrival. We used the following matlab short script to pick, plot, and save the data:

```
clear all; clc;
format long g;
cd /Users/saadansi/Desktop/Ref10000/Int1hfrf/Interval1Q20/1000
a=load('outfile');
b=a(:,2);
c=a(:,3);
[d,e]=max(c(8192*2+1:8192*3));
f=b(8192*2+1:8192*3);
g=f(e);
[h,i]=min(c(8192*2+1:8192*3)); j=b(8192*2+1:8192*3);
k=f(i);
oba=[g,d,k,h]; l=a(8192*2+1:8192*3,1:3);
plot(l(:,2),l(:,3))
saveas(gcf,'Int1Q20F1000-z-comp.fig');
cd /Users/saadansi/Desktop/picking/
fid = fopen('IntervalOnePicks','a+');
fprintf(fid,'%6.10e ' ,oba');
fprintf(fid,'\n');
```

Appendix B

Seismograms Calculated Using DWN

This appendix contains three seismograms with central frequencies, 500,2500, and 5000, respectively, and a varying Q for each of the intervals of interest.

B.1 Interval One

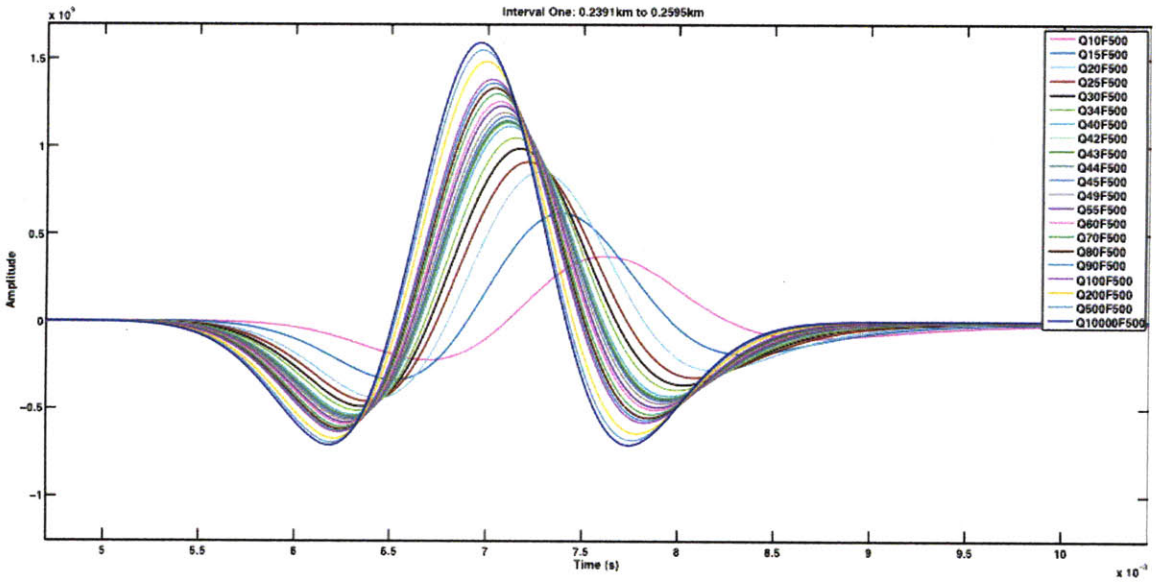

Figure B.1: Overlaid seismograms over a range of Q for central frequency 500

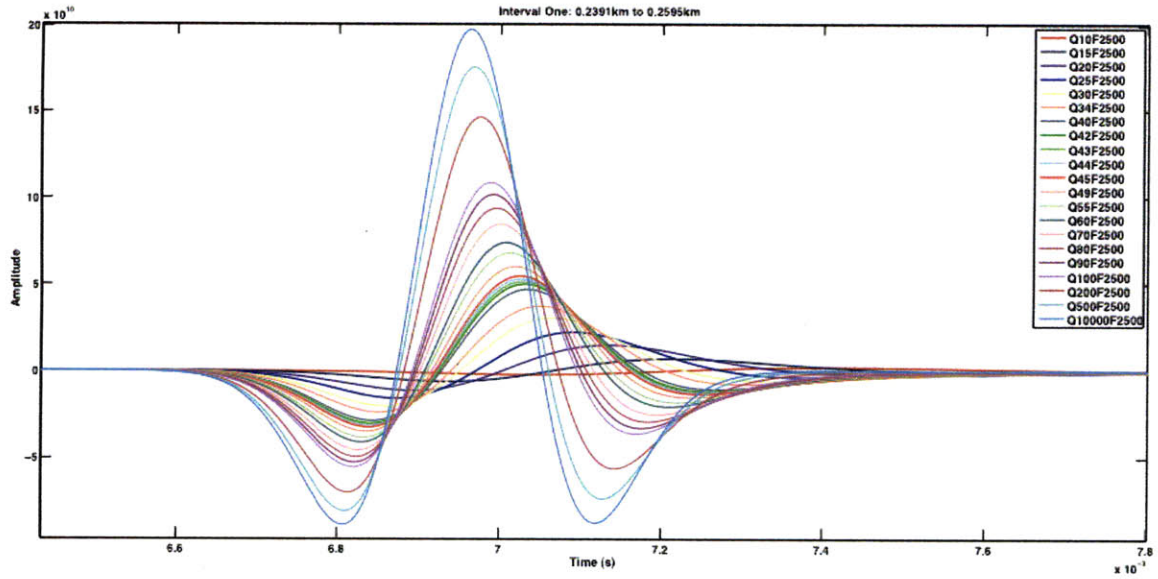

Figure B.2: Overlaid seismograms over a range of Q for central frequency 2500

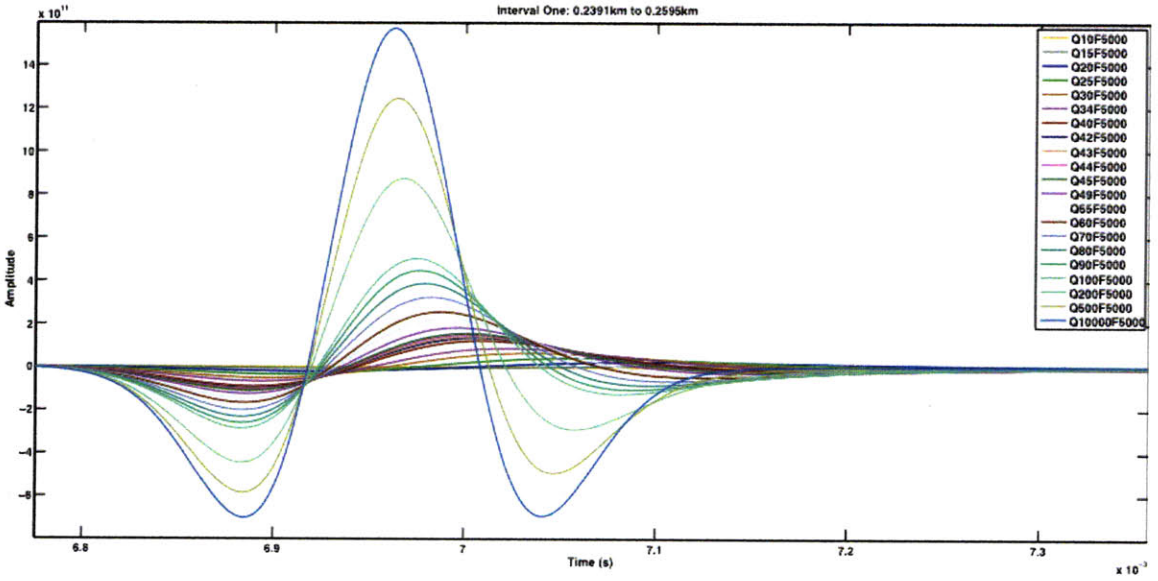

Figure B.3: Overlaid seismograms over a range of Q for central frequency 5000

B.2 Interval Two

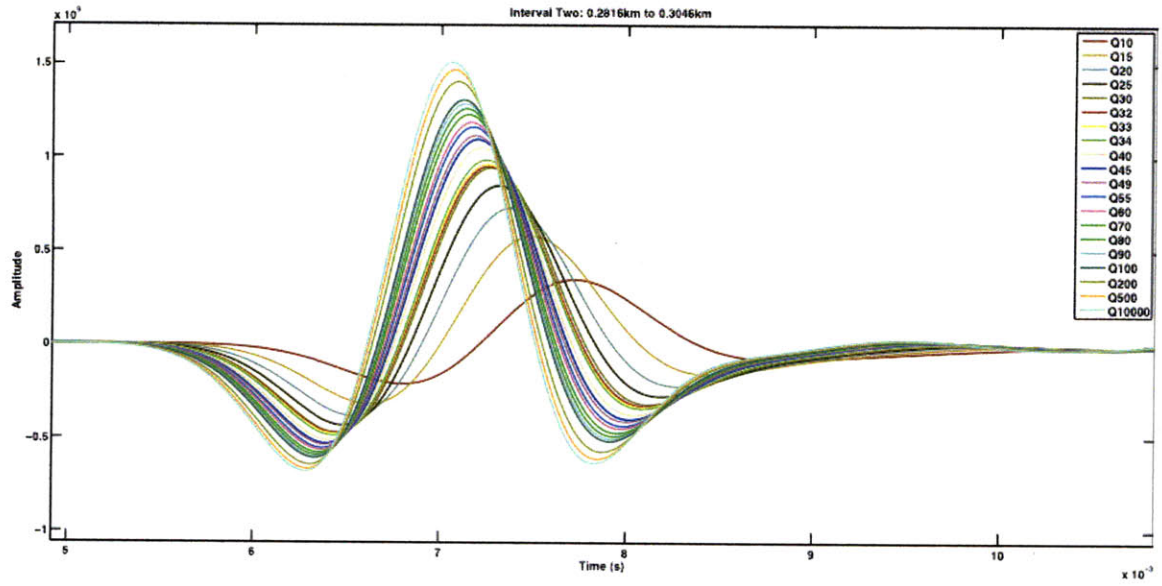

Figure B.4: Overlaid seismograms over a range of Q for central frequency 500

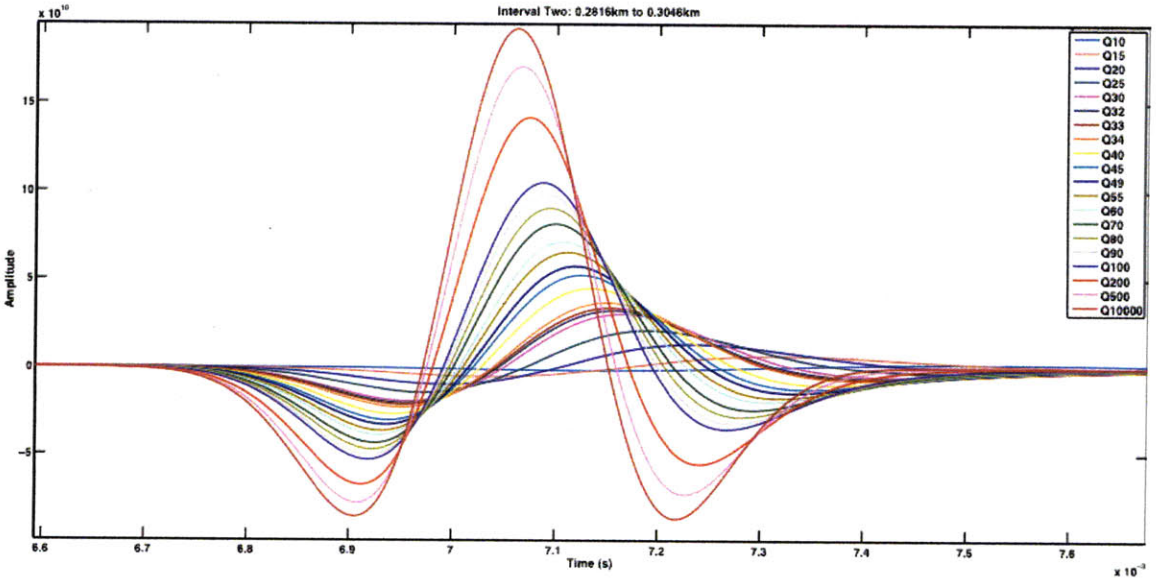

Figure B.5: Overlaid seismograms over a range of Q for central frequency 2500

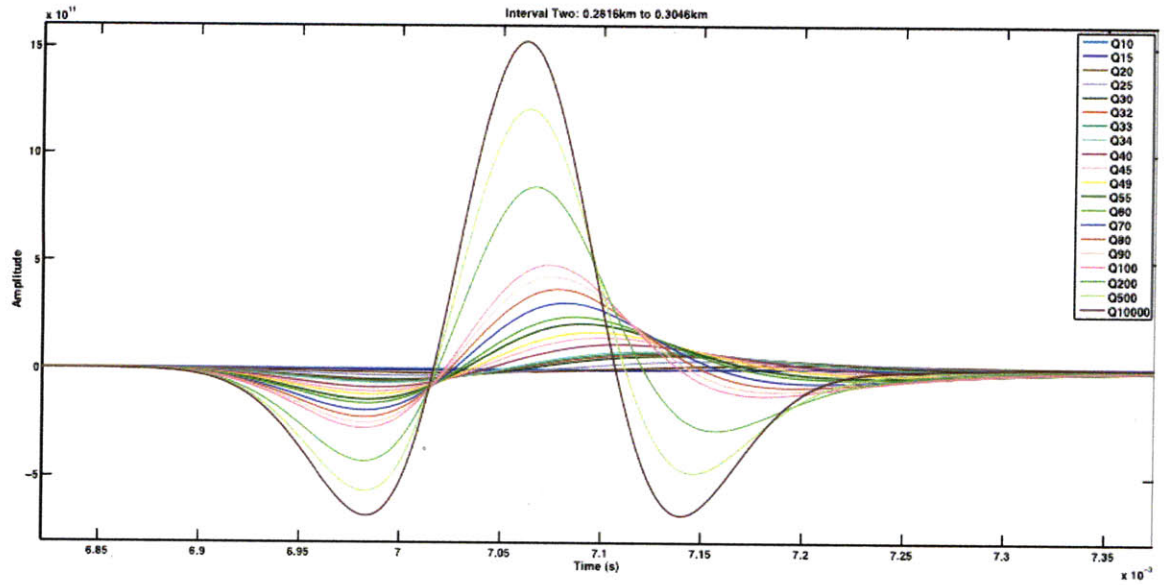

Figure B.6: Overlaid seismograms over a range of Q for central frequency 5000

B.3 Interval Three

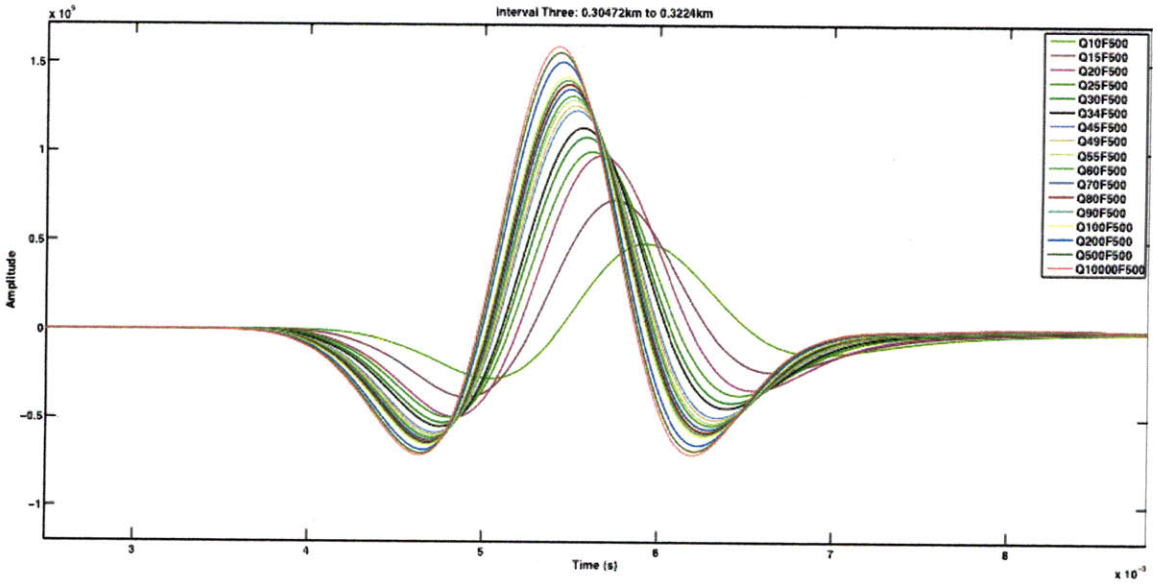

Figure B.7: Overlaid seismograms over a range of Q for central frequency 500

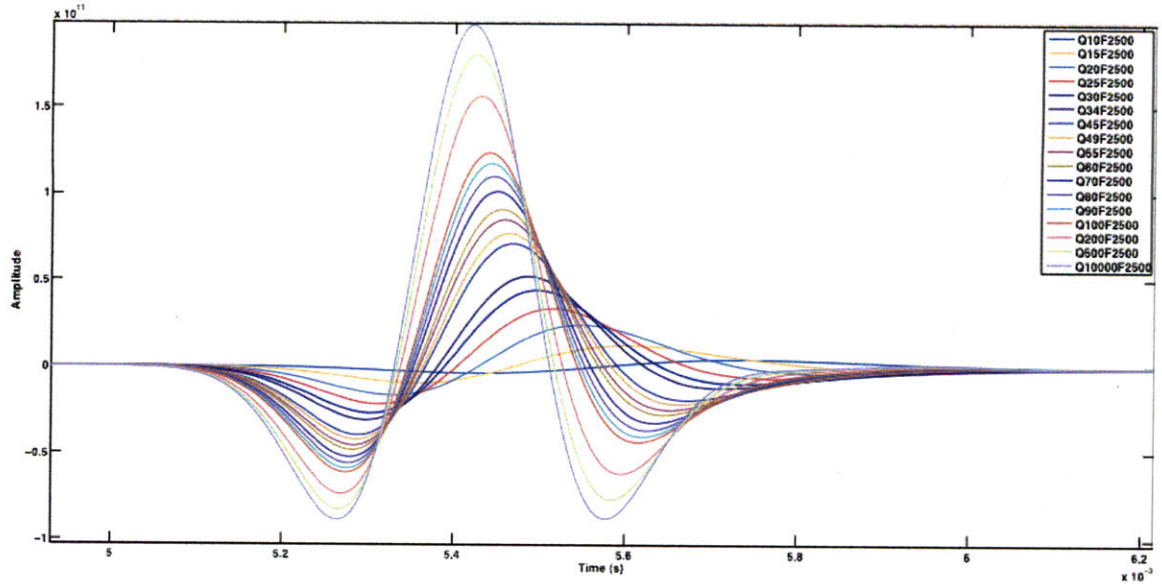

Figure B.8: Overlaid seismograms over a range of Q for central frequency 2500

B.4 Interval Four

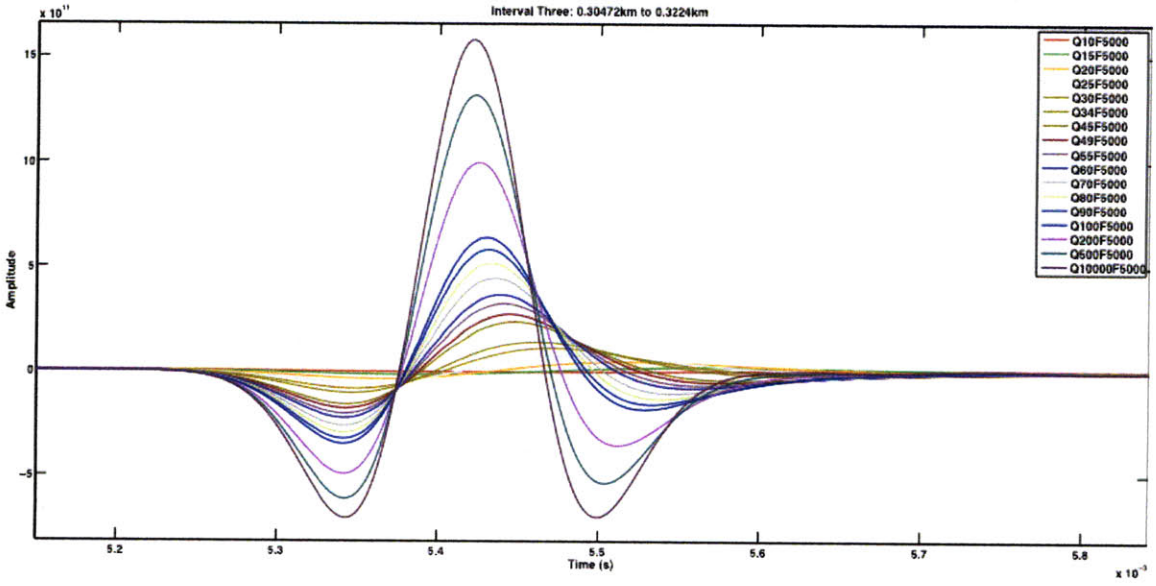

Figure B.9: Overlaid seismograms over a range of Q for central frequency 5000

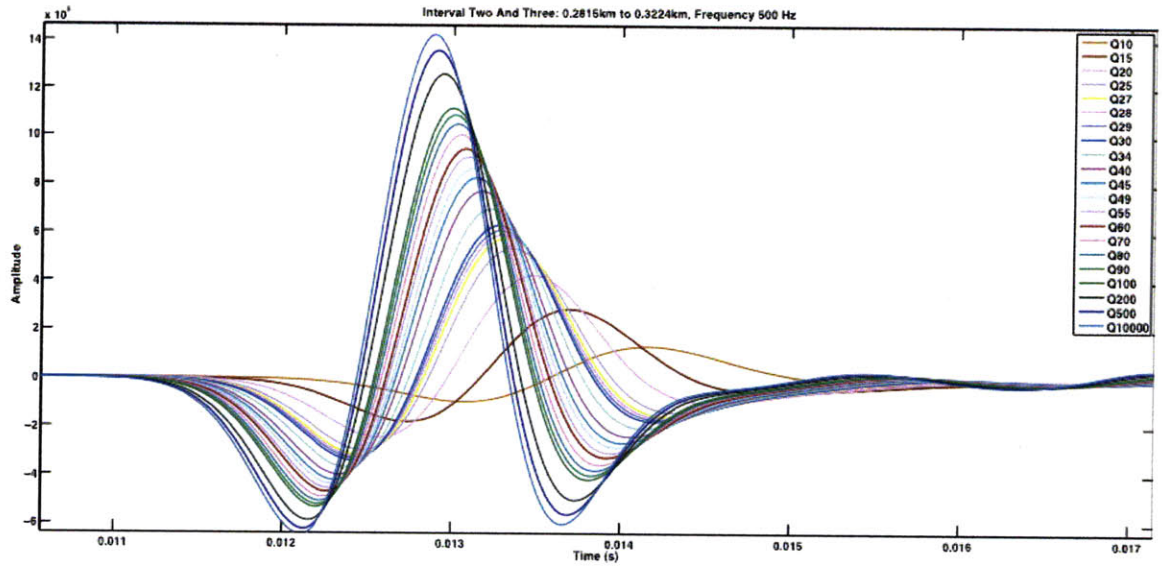

Figure B.10: Overlaid seismograms over a range of Q for central frequency 500

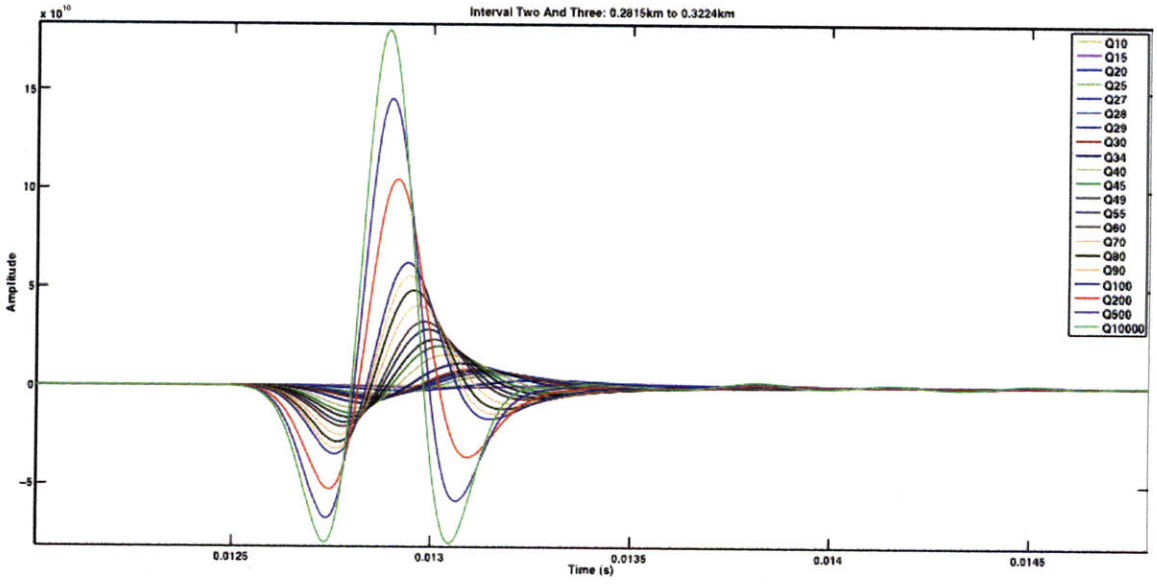

Figure B.11: Overlaid seismograms over a range of Q for central frequency 2500

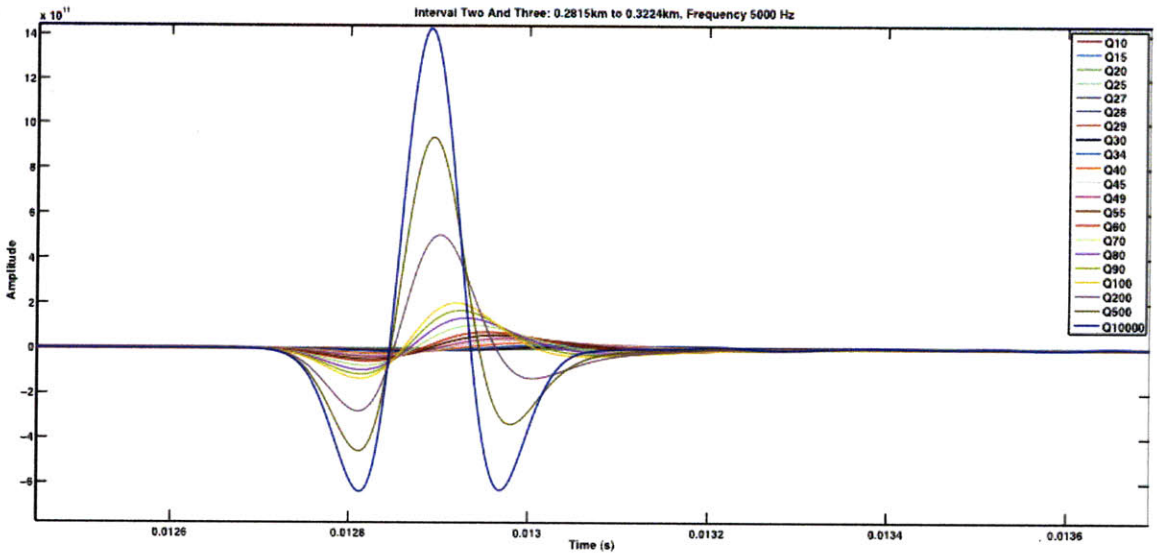

Figure B.12: Overlaid seismograms over a range of Q for central frequency 5000